Escola de Camins
Escola Tècnica Superior d'Enginyeria de Camins, Canals i Ports
UPC BARCELONATECH

Production and optimization of an UO$_2$ electrode by electrodeposition to perform corrosion studies in hyper-alkaline conditions with calcium and silicium electrolytes

Treball realitzat per:
Karina Torres-Rivero Andrade

Dirigit per:
Joan de Pablo

Màster en:
Enginyeria Ambiental

Barcelona,

Departament de Camins y Ports de Barcelona

TREBALL FINAL DE MÀSTER

Summary

The nuclear waste generated due to the production of electricity is confined into isolated repositories. Because of the use of cement in the isolation barriers and also its use as sealing material, it is important to study the effect of cementitious waters in contact with the spent fuel, since these materials might play an important role as physical and chemical barriers to the release of radionuclides into the far field. A review of the UO_2 electrodeposition process was done to modify commercial electrodes (Dropsens), subsequently to perform electrochemical experiments and therefore understand the behavior of fuel matrix in hyper-alkaline conditions, with Ca and Si dissolutions. Two deposition times were used, 15-min and 60-min; the most reproducible results were shown by the 60-min electrodeposited electrode and this was used for the rest of the experiments. Following this, cyclic-voltammograms were recorded using three types of electrolytes: Na^+Cl^- 0,1 M; Na^+Cl^- 0,1 M, SiO_3^{-2} 0,001M; Na^+Cl^- 0,1 M, SiO_3^{-2} 0,001M and Ca^{2+} 0,0001 M, all with pH=12. Potentiostatic and corrosion potential experiments were performed to determine the effect of the Ca and Si ions in the oxidation process. The CVS showed six defined regions where oxidation and reduction process occurred; the potentiostatics results revealed the highest current density was obtained for SiO_3^{-2} and Ca^{2+}, SiO_3^{-2}, and the lowest current density was obtained for Na^+Cl^-. The corrosion potential value obtained for Na+Cl- was 42 mV, 40 mV for SiO_3^{-2} and -2 mV for SiO_3^{-2}, Ca^{2+}. These results exhibit that both ions reinforce the formation of protective corrosion products on the surface electrode, working as inhibitors and/or blocking the fuel corrosion process.

Resumen

Los residuos radioactivos generados debido a la producción de electricidad están confinados en repositorios aislados. Puesto que el cemento es usado en las barreras de aislamiento, así como material de sellado, es importante estudiar el efecto de las aguas cementosas en contacto con el combustible usado ya que estos materiales pueden jugar un rol importante como barreras químicas y física para la liberación de radionuclideo en el entorno. Se realizó una revisión del proceso de electrodeposición del UO_2 para modificar electrodos comerciales (Dropsens). Ello permitió realizar experimentos electroquímicos y así como comprender el comportamiento de la matriz de combustible

en condiciones hiper alcalinas con disoluciones de Ca y Si. Se usaron dos tiempos de deposición: 15-min y 60-min; los resultados más reproducibles fueron obtenidos por el electrodo electrodepositado en 60-min así que este fue usado para realizar el resto de los experimentos. Se registraron ciclo-voltamogramas usando tres tipos de electrolitos: Na+Cl- 0,1 M; Na+Cl- 0,1 M, SiO3-2 0,001M; Na+Cl- 0,1 M, SiO3-2 0,001M y Ca2+ 0,0001 M, todos ellos a pH=12. Se realizaron experimentos potencioestáticos y de potencial de corrosión para determinar el efecto de los iónes Ca y Si en el proceso de oxidación. Los CVS mostraron seis regiones definidas donde ocurrieron los procesos de oxidación y reducción, los resultados potencioestáticos revelaron que la densidad de corriente más alta fue obtenida para el SiO_3^{-2} y Ca^{2+}, SiO_3^{-2}, y la densidad de corriente más baja fue obtenidapara el Na+Cl. El valor del potencial de corrosión obtenido para Na^+Cl^- fue de 42mV, 40 mV para el SiO_3^{-2} y -2 mV para el SiO_3^{-2} y Ca^{2+}. Estos resultados demuestran que ambos iones refuerzan la formación de productos de corrosión protectores en la superficie del electrodo, actuando como inhibidores y/o bloqueando el proceso de corrosión del combustible.

Acknowledgements

First, I would like to thank my thesis advisor, Joan de Pablo of the EEBE at UPC Campus Diagonal-Bèsos. The door to to Prof. de Pablo was always open whenever I ran into a trouble spot or had a question about my research or writing.

I would also like to thank to experts who were involved in the development of this thesis: Dra. Alexandra Espriu-Gascón and Dr. Julio Bastos, without their participation this investigation could not have been successfully conducted.

To my beloved husband, my unconditionally support. Thank you for all your patience and love. I love you.

To my parents and my sister, for being there when I needed them. Thanks to them I'm here doing what I like the most.

To my friends: Silvia, Júlia, Sònia, Ana Julia and specially Josep and Lulú for listening to me when I needed the most. Without you, this master wouldn't have been the same.

To God, for letting me have my precious family, husband all my friends to support me in the most difficult times.

Un ser sin estudios es un ser incompleto…

Simón Bolívar

Index

Acronym List

CTSF: Centralized temporary storage facility

CV: Cyclic voltammetry

DGR: Deep Geological Repository

FAC: Flow-assisted corrosion

HLW: High-level waste

IAEA: International Atomic Energy Agency

IASCC: Irradiation-assisted stress corrosion cracking

IRF: Instant release fraction

LLW: Low-level waste

LOAEL: Lowest

SCC: Stress corrosion cracking

SEM: Scanning electron microscopy

SNF: Spent Nuclear Fuel

SPEs: Screen printed electrodes

TEM: Transmission electron microscopy

TRU: Transuranic

XPS: X-ray photoelectron microscopy

Figure List

Tables List

1. Introduction

Today nuclear fuels are mostly based on uranium. Through a series of steps an efficient fuel to generate electricity is produced after the uranium enrichment by the conversion of UF_6 to UO_2 (IAEA, 2011).

The nuclear power stations generate electrical energy from fission nuclear processes. The nuclear fission releases heat and energy that is transformed in electricity. The waste generated keeps its natural cycle of radioactive disintegration (Fernández, 2011).

It is considered nuclear waste all product or waste material which presents radioactivity traces and for which it is not planned any use; it includes solids, liquids and residuals polluted gases (Fernández, 2011).

The nuclear fuel cycle is shown in figure 1 which represents the progression of nuclear fuel from creation to disposal.
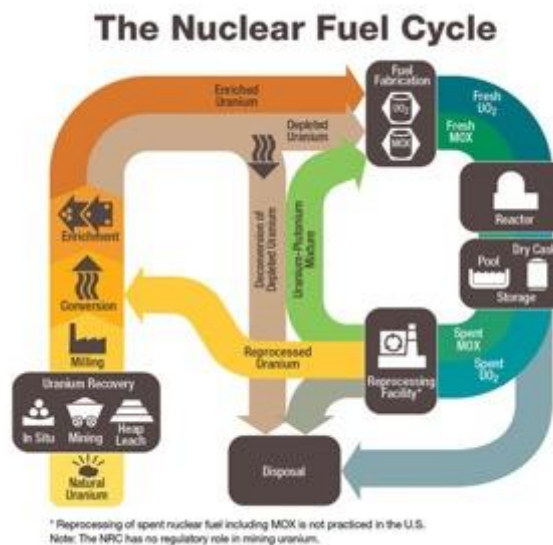
Figure 1. The nuclear fuel cycle. The complete process: from creation to disposal. IAEA, 2011.

The first step is the *uranium recovery*. This phase focuses on extracting natural uranium ore from the Earth and concentrating that ore. The recovery operations produce a product called, "yellowcake" (U_3O_8), which is then transported to a fuel cycle facility.

Most of the nuclear plants require fuel with U-235 enriched to a level of 3-5%, hence uranium must be enriched to increase the concentration of U^{235}. Because of that, the yellow cake, is converted to uranium hexafluoride (UF_6), here is where the *uranium conversion* takes place.

The *enrichment process* is the following phase, where isotope separation takes place, through a gaseous diffusion process. Because the smaller U-235 isotopes travel slightly faster than U-238 isotopes, they tend to leak (diffuse) faster through the porous membrane walls of a diffuser, where they are collected and concentrate (IAEA, 2011). In the following table a comparison of radioactive properties of uranium isotopes is shown.

Table 1. Comparison of radioactive properties of uranium isotopes (ANL, 2001)

Isotope	Half-Life (years)	Natural abundance (%)	Specific activity (*Ci/g*)	Decay mode	Radiation Energy (*MeV*)		
					Alpha (α)	Beta (β)	Gamma (γ)
U-232	72	0	22	α	5,3	0,0017	0,0022
U-233	160000	0	0,0098	α	4,8	0,0061	0,0013
U-234	240000	0,0055	0,0063	α	4,8	0,013	0,0017
U-235	700 million	0,72	0,0000022	α	4,4	0,049	0,16
U-236	23 million	0	0,000065	α	4,5	0,011	0,0016
U-238	4.5 billion	≥99	0,00000034	α	4,2	0,010	0,0014

As the table 1 shows, the main isotopes of uranium have extremely long lifetimes except for uranium 232, all of them are alpha emitters of 4 to 5 MeV of energy. The columns referred to gamma radiation show the presence of a low energy gamma radiation and rare decays beta. Specific activities (activities reduced to 1 gram) are inversely proportional to half-lives (ANL, 2001).

Once the enrichment process is completed, the following process is the *deconversion*, which consists in the chemically extraction of the fluoride atoms from the DUF_6 and

replaces them with oxygen to produce uranium dioxide (UO_2). Then the *fuel fabrication* is the next step, where the fuel is created in the form of ceramic pellets. These are formed from pressed UO_2 at high temperature (over 1672 K). The pellets are then encased in metal tubes of zircaloy to form fuel rods, which are arranged into a fuel assembly ready for being introduced into a nuclear reactor for energy production.

Next, the *interim storage* takes place. Here, the spent nuclear fuel (SNF) is stored under water, which provides both cooling and radiation shielding. A *reprocessing* step can follow the interim storage, where the SNF is separated from the nuclear materials that may be recycled. The final step is the disposition of high radioactivity level waste.

Disposal of nuclear wastes has been studied for long time under the auspices of different American and European agencies. The main purpose of these organizations was to design and construct facilities that would accept and start disposing of spent nuclear fuel and high-level wastes.

Radioactive waste management is an integrated system that involves several activities: accumulation, processing, handling, packaging, transportation, storage, disposal, decontamination and decommissioning of the spent nuclear fuel (Saling et al. 2001).

In Spain, the nuclear waste management both from nuclear power stations and those generated by other radioactive facilities such as hospitals and research centers, is overseen by National Company of Radioactive Waste (ENRESA, for its acronym in spanish). The way to dispose the nuclear waste is by classifying it by its level of radioactivity.

There are two different management strategies for spent nuclear fuel (IAEA, 2006). In the first one the fuel is reprocessed to extract usable material (uranium and plutonium) for a new fuel. In the other one, the spent fuel is simply considered as a waste and is stored in a temporary disposal and later in a final repository.

This thesis is focused on the second management strategy in order to study processes involved in the spent nuclear fuel alteration under storage conditions where the waste is confined. Also, concrete can be found in the repository as a barrier and it also can be used as sealing material in the deep geological repository (DGR).

Assessing the performance of spent nuclear fuel in a potential future geological disposal system requires the understanding and quantification of the important time-dependent

phenomena influencing its behaviour on a time-scale up to millions of years. Such a demanding goal requires the development and qualification of models predicting the spent fuel matrix dissolution.

This lead us to define the general objective and the specifics objectives of this thesis, which are the following:

1.1 General Objective

Development and optimization of dioxide uranium electrodes for the electrochemical characterization of spent nuclear fuel in order to develop a model for predicting the behaviour of the fuel in the conditions expected in a final repository.

1.2 Specifics Objectives

- Surface modification of a commercial electrode (Dropsens) by UO_2 electrodeposition.
- To perform electrochemical measurements by doing cyclic-voltammogram analysis, pontenciostatic tests and corrosion potential measurements.
- To perform surface analysis by scanning electron microscopy (SEM), X-ray photoelectron spectroscopy (XPS) and RAMAN spectroscopy

2. Storage and Disposal of spent nuclear fuel and high level waste

The fundamental design objective of geological repositories is to confine the waste and to isolate it from the environment.

Most of the countries, which must manage nuclear spent fuel, incorporate the following basic technical principles to their developed disposal concepts (IAEA, 2006):

a.- Encapsulation of spent fuel or HLW in a tight canister with a very long expected lifetime.

b.- Assurance that the conditions in the repository will allow the canister to remain intact and tight for as long as possible. These conditions include: mechanical stability stable geochemical conditions and very limited groundwater movement that could bring corrosive agents in contact with the canister.

c.- Backfilling of the repository with appropriate materials and adequate geological media.

The main characteristics of the spent fuel and high level waste disposal are the long-lived radioactivity of the SNF and HLW (high level waste), its heat generation and its radiation level (IAEA, 2006).

Normally, the heat generation determines the amount of waste that can be confined in a determined volume of rock. Waste with high radiation levels requires to be shielded, and depending of the amount of long-lived radioactivity isotopes, the safety of a repository must be considered looking forward for tens to hundreds of thousands of years.

In this section, we pretend to describe the characteristics of the spent nuclear fuel, including the process that affect the dissolution of fuel matrix, chemistry and the release process of the radionuclides. Also, the disposal concept, all the phases to confine nuclear waste and its characteristics are described.

2.1 Classification by type and Level of Radioactivity

Nuclear spent fuel is defined as waste material that is contaminated with alpha-emitters radionuclides of sufficiently long life (>20 years) of elements with atomic number 92 or larger and concentrations greater than 100 nanocuries per gram.

Spent nuclear can be classified according to the origin, the type of material present and their level of radioactivity, as follows (Saling et al. 2001):

1. *High-level waste (HLW)* is the result from the reprocessing of spent fuel from a defense or commercial reactor. The amount of plutonium and other heavy isotopes remaining in the solutions is small, about 0,5% of original Pu and U; the residue consists mainly of fission products.

2. *Spent Nuclear fuel (SNF)* discharged from the reactor may be stored at the reactor site and eventually placed in a waste repository without reprocessing. SNF will be treated as a HLW unless and until it is retrieved and reprocessed at a future time. In this document, we are going to discuss primarily this type of radioactive waste. The spent fuel contains uranium (96%), plutonium (1%) and high level waste products (3%). The uranium, with less than 1% fissile U-235 (IAEA, 2011).

3. *Transuranic (TRU)* includes all transuranic nuclides except ^{238}P and ^{241}Pu and also includes ^{233}U and its daughter products (Jensen, 1983).

4. *Low-level waste (LLW)* this waste often has relatively little radioactivity and contains practically no TRU elements. Most LLW requires little or no shielding, may be handled by direct contact, and may be buried in near-surface facilities.

5. *Mill tailings* from uranium mills constitute another type of waste with a low level of radioactivity, but they are not classified as LLW. The tailings contain elements such as thorium and radium, which are by-products of the decay of ^{238}U and are not removed in the extraction of uranium.

Most of the radioactivity is associated with the commercially generated SNF and is primarily generated in commercial reactors. The following table (table 2) shows a summary of nuclear waste types and sources.

Table 2. Nuclear waste types and sources (Saling et al. 2001)

Source	Nuclear waste type			
	Spent nuclear fuel (SNF)	*High-level waste (HLW)*	*Transuramic (TRU)*	*Low-level waste (LLW)*
Commercial nuclear fuel cycle operations	x	X		x
Institutions (hospitals, universities, etc.)	x		X	x
Industrial users	x		X	x
Decontamination and decommissioning of fuel cycle			X	x
Defense-related activities	x	X	X	x

In Spain, the ultimate decision for nuclear waste treatment is made by the Government based on the researches that have been made, which focus on (Fernández, 2011):

- **Separation and transmutation**. This method is known as closed cycle, which permits to manipulate the spent fuel to separate and transmute certain long life radionuclides; after this process, these can be reused as energetic materials, reducing the waste inventory at the same time.
- **The DGR: Deep Geological Repository**. This method is open cycle, in which the HLW and SNF are storage underground and deep, in a repository.

Nowadays, the Spanish Government has chosen for a Centralized Temporary Storage Facility (CTSF) (ATC for its acronym in Spanish).

The CTSF is a storage system designed to house the SNF and HLW from nuclear power plants for a given period. These facilities are located on the surface or at a depth of relatively few meters, in consequence, they require continuous monitoring and control measures. In this sense, the Centralized Temporary Storage Facilities are the most ideal temporary solution from safety reasons, since they allow the monitoring measures to be concentrated on a single facility. The research results show that this option can guarantee the storage of spent fuel for a period of 50 years. In any case the temporary

facilities cannot be considered the definitive solution and cannot be extended indefinitely (Consejo de Seguridad Nuclear, Gobierno de España, 2015).

Because of the previously reason, in Europe, the DGR option is the most considered option as viable solution for nuclear waste long-term storage.

2.2 Geological Formation

The DGR is based on the multi-barrier principle, which consists in interposing a series of artificial and natural barriers between the nuclear waste and the biosphere. Generally, the SNF from the nuclear power plants is ceramic pellets with 95% of UO_2 stables and slightly soluble which is considered as a barrier itself (first barrier), due to its physicochemical form. The residue is encapsulated in a carbon steel canister (second barrier). The canister is introduced into the galleries and it is surrounded by a compacted clay barrier, so-called, bentonite. The main purpose is to ensure that the travel time of any stored radionuclide is long enough, so its radioactivity had decay and cannot modify any natural radioactive level (Astudillo, 2001).

The repository should be placed in a stable geological formation; deep saline, granite a clay formations should be considered. If the geological formation chosed is a clay formation, it is necessary to introduce a concrete barrier which is going to act as a structural support for the disposal facility (Fernández, 2011).

The nuclear waste must be store in a series of connected galleries, that would be constructed at a depth between 300 and 1000 meters from the surface, in order to prevent the flow of groundwater and ensure a safe distance to the biosphere.

The structure and composition of the various type of spent fuel have been investigated from the perspectives of reactor operation and geologic disposal. At the end of the fuel's useful life in the reactor, about 95% of the spent nuclear fuel still consists in UO_2 (Bruno et al. 2006).

In the assessment of the concept of the direct disposal of irradiated nuclear fuel, an important objective is to predict the release rate of radionuclides from the fuel under the conditions anticipated in a nuclear waste vault. Studies of the dissolution is initially

independent of matrix dissolution, with a small fraction of certain fission products (e.g. [137]Cs) being released rapidly on exposure of the fuel to the water (Sunder et al. 1991).

2.3 Spent Nuclear Fuel Characteristics

For more than fifty years, uranium dioxide was world-wide used as the main fuel for two generations of nuclear power plants. There are number of different types of fuel, but they are predominantly uranium based, mainly UO_2 or, in some cases, metallic U.

Chosen first as the most convenient uranium compound for easy fabrication of sintered pellets, UO_2 displayed in the long run an excellent combination of thermophysical properties as well as an uncommon resistance to burn-up and radiation damage (Ronchi et al. 2011). A high level of proficiency has been reached by using this type of fuel, but certain preoccupation was originated after careful observations of the transformations in the highly irradiated nuclear fuels (Jovani-Abril, 2014).

Prior to irradiation in a reactor, UO_2 fuel consists of fine grained (3-10 μm) pellets with very high-density and high-purity of UO_2 (Johnson and Werme, 1994).

After irradiation to burnups from 8 to 40 MW d/KgU (Jonhson and Werme 1994), anywhere from 1 to 4% of the uranium will have been fissioned to produce a wide variety of stable and radioactive fission products (Jonhson and Werme 1994).

Many of these products are insoluble in UO_2 and can form precipitates within grains and at grains boundaries. Another fraction of the products are gases, like Xe and Kr, some elements that are volatile at fuel operating temperatures (eg., Cs and I) and metal such as Tc, Mo, Ru, Rh and Pd. Also, it contains fission products that occur as oxide precipitates of Rb, Cs, Ba an Zr; fission products that form solid solutions with the UO_2 fuel, such as Sr, Zr, Nb, and the rare-earth elements; transuranium elements that substitute for U in the UO_2.

In figure 2, the microstructure of the spent fuel is shown. The high temperatures experienced during in-reactor irradiation allow that the most insoluble species diffuse out from the grains to the grain boundaries. A fraction of total content of noble gas and volatile fission products accumulate there, and can be released to the periphery of the fuel because of, the formation of fission gas tunnels at grain boundaries and cracks in the pellets.

The fission products can be released from grain boundaries during in-reactor irradiation, leading to their accumulation at the cooler gap between the fuel and the cladding.

Other microstructural features that may affect fission-product release include grain growth in the hot central region of the fuel, and the subdivision of grains that occurs in the cool outer region of the fuel.

The burn-up is also not uniform across the fuel pellet, higher burn-ups can increase porosity and polygonization of the UO_2 grains, reducing the size to 0,15 μm, this is the "rim effect" (Bruno et al. 2006).
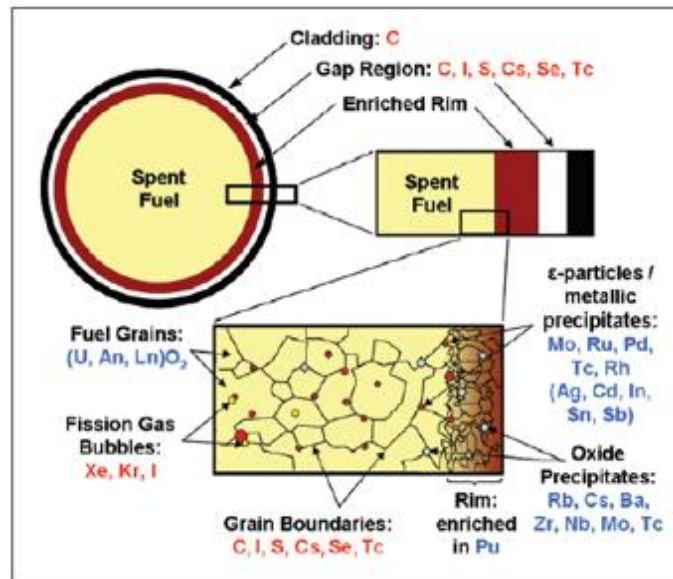
Figure 2. Illustration of the microstructure of spent fuel and the distribution of actinides and fission products following burn-up in a reactor. Red labels indicate instantaneous release upon contact with water, blue indicates slower release rates. Bruno et al. 2006

It is important to study the microstructure of the spent fuel, in order to understand the impact on the release of contained fission products, and the dissolution behavior of spent fuel and of UO_2, the principal constituent of the fuel (Johnson and Werme, 1994) (Bruno et al. 2006).

2.3.1 Processes controlling fuel Matrix Dissolution

The performance assessment of the final disposal of the spent nuclear fuel in the DGR is strongly dependent on the spent fuel matrix dissolution. (Casas, de Pablo y Rovira, 2014; Berner, 1992). Because of this, a description of the processes that affect the dissolution of the UO_2 in the fuel matrix is shown as following.

- **Radiolysis of water by the alpha, beta and gamma radiation**

The radiolysis of water by the alpha, beta and gamma radiation could reach the interface between the fuel surface and aqueous solutions. Under an ambient with reducing conditions, radiolysis can create oxidizing conditions at the surface of the fuel. While under oxidizing conditions, radiolysis is much less important (Bruno et al. 2006).

Since alpha activity within spent fuel decays very slowly compared to gamma and beta activity, there is a possibility that oxidative dissolution will be sustained by alpha radiolysis for a long period of time (Shoesmith and Sunder, 1991).

- **Oxidants produced during radiolysis**

The oxidants produced under oxidizing conditions, have a strong tendency to oxidized the surface of the UO_2 to UO_{2+x}. The oxidizing species are taken up by the fuel surface, and additional oxygen atoms enter the UO_2 structure as interstitial oxygens, in consequence, the fuel reaches a composition of UO_{2+x} (0,3<x<0,4) (Bruno et al. 2006). This dissolution process is considered as a corrosion reaction, in which the oxidant is consumed to convert the insoluble U^{IV} (in UO_2) to the much more soluble U^{VI} (as UO_2^{2+}) (Shoesmith, 2007).

- **The oxidized U(VI) at the fuel surface**

The oxidized U (VI) at the fuel surface can be released by complexing compounds present in groundwater. The initial composition of the groundwater can be modified due to its concentration during evaporation or reaction with backfill and the metal waste package.

Uranium (VI) has a strong tendency to form complexes in solution with oxygen-containing ligands. In geological disposal conditions, the main oxygen-containing ligands are HCO_3^- (bicarbonate) and hydroxide (OH^-).

If the concentration of U(VI) increases and the water saturation is reached, secondary U (VI) phases can precipitate under oxidizing conditions.

2.3.2 Chemistry of UO₂ dissolution

The dissolution of UO_2 has been studied under oxidizing conditions (Shoesmith, 1991; de Pablo et al. 1996). In the presence of radiolytically decomposed water, many reactions can occur on the fuel surface including oxidative dissolution, radical combination, hydrogen peroxide decomposition, reduction of oxidized surface layers, and radical recombination catalyzed by redox-active species in the surrounding environment (Shoesmith, 1991).

The following figure (fig. 3) shows the chemistry of UO_2 dissolution as a function of electrochemical potential. The potential scale in this figure represents the redox condition established at the UO_{2+x} surface ($0 < x < 1$), not the redox potential in the near environment solution. It is a measure of the kinetic balance between the anodic (oxidation) and cathodic (reduction) reactions that can occur on the surface (Shoesmith, 1991).
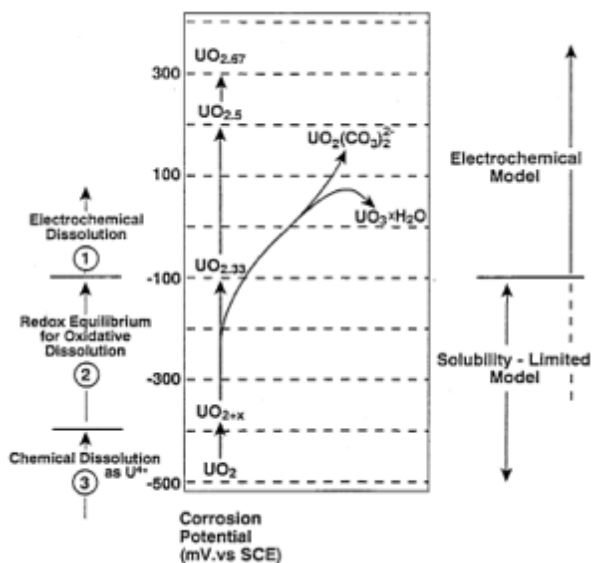
Figure 3. **Surface chemistry of UO₂ oxidation/dissolution as a function of surface redox conditions. Sunder et al. 1997.**
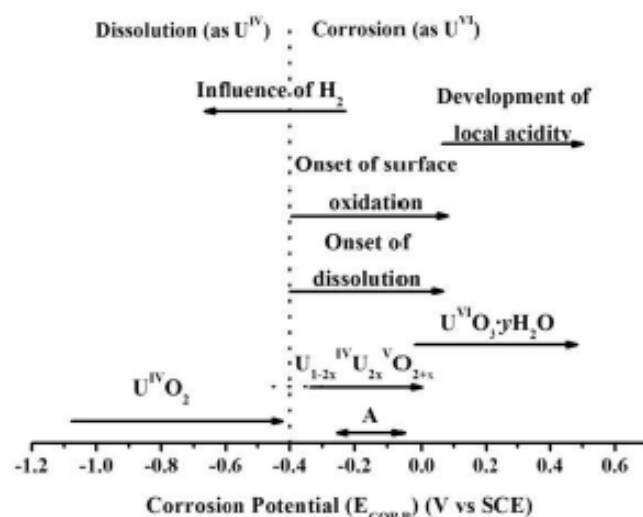
Figure 4. **Surface chemistry of UO$_2$ oxidation/dissolution as a function of surface redox conditions. Shoesmith, 2007**

The figures above (fig. 3 and 4), show the composition of a UO$_2$ surface as a function of potential vs SCE. -400 mv is the potential threshold above which UO$_2$ would be expected to be subject to corrosion, and below which only chemical dissolution can occur. The arrow A indicates the corrosion potential range predicted by a mixed potential model to describe fuel corrosion due to the alpha radiolysis of water inside a failed waste container (Shoesmith, 2007). The upper limit is supposed to be the corrosion potential (E$_{corr}$) if the container fails on emplacement, and the lower limit correspond to the E$_{corr}$ predicted after 10^6 years (Shoesmith, 2007).

The stability of UO$_2$ is very dependent on vault redox conditions. At reducing conditions, which are expected in deep groundwater, the dissolution of UO$_2$-matrix can be explained in terms of solutions, while oxidizing conditions, the UO$_2$ is thermodynamically unstable.

2.3.3 Radionuclides release mechanisms

The release of more than 90% of radionuclides contained in the used fuel matrix will be governed by the corrosion/dissolution of the UO$_2$ matrix. It is possible to relate the rate of this process with the solubility of uranium in the groundwater. Under DGR conditions, groundwater is anoxic and any available oxygen will be rapidly consumed by mineral and biochemical reactions in the surrounding clays (Shoesmith, 2007). While groundwater entering to the failed container may be oxygen-free, its radiolysis

due to the residual radioactivity from the fuel will produce a variety of chemical species including oxidants (Shoesmith, 2007) (Johnson et al. 1996).

The performance assessment of the final disposal of the spent nuclear fuel requires a profound knowledge of the different radionuclides release mechanisms contained in the nuclear waste fuel when they get in contact with the groundwater. These mechanisms are explained as follows:

1. **Instantaneous release at the time of waste package failure**

This generally referred to as the instant release fraction (IRF), which is the fraction of the inventory rapidly released and with faster relase rate than the matrix when the metal canister is breached. The radionuclides of most interest during this rapid release are mainly the fission gases, such as Xe and Kr, and the volatile elements, such as I, Cs and Cl (Bruno et al. 2006).

2. **Fission products release from grain boundaries**

Jonhson and Werme (1994) studied an intergranular fracture surface of a spent fuel sample using X-ray photoelectron spectroscopy, the study shows the buildup of insoluble fission products at grain boundaries. The fission products such as Cs, Rb, Ba and Te can be released from grain boundaries during in-reactor irradiation, leading to their accumulation at the cooler gap between the fuel and the cladding.

3. **The much slower, long-term release that results from the alteration and dissolution of the fuel matrix, usually UO_2**

The important processes include: (1) oxidation of the U(IV) to U(VI) and the formation of higher oxide structures on the fuel surface and at grain boundaries; (2) bulk dissolution of the UO_2 and release of radionuclides (e.g. Pu and Np) that substitute for U; (3) dissolution of segregated oxides and immiscible metallic alloys in the fuel grains; (4) the formation of secondary alteration products, such as coffinite ($USiO_4$) under reducing conditions or U (VI) phases, like becquerelite or uranophone under oxidizing conditions (Burns and Klingesmith, 2006). The chemical reactions depend on groundwater composition and flow rate. Thus, the release of radionuclides from SNF can only be understood in the context of coupled near-field processes, which include interactions among the corrosion products of waste package, percolating groundwater, and the surrounding rock (Bruno et al. 2006)

2.4 Metal Canister

The metal canister can be designed for both purposes: storage and transportation. In case of storage, the shielding is provided primarily by the cask structural material, which may be forged steel, nodular cast iron or composite materials.

A metal canister consists of the following components (IAEA, 2009):

- A basket assembly, which transfers heat to the cask body wall and provides neutron absorption.
- The containment vessel, which consists of an inner shell and is usually a welded, carbon steel cylinder. There are two holes through the containment vessel: one is for draining and the other is for venting.
- A gamma shield around the walls and bottom of the containment vessel, which is welded to the closure flange.
- A neutron shield surrounding the gamma shield.
- A protective cover for weather protection for the closure lid and seal components.

2.5 Compacted Clay Barrier

This type of barrier is made of clay materials. Among them, bentonite is one of the considered materials due to its ideal physicochemical characteristics and crystalline structure. Bentonite is a phyllosilicate that permits to hold radionuclides that could escape from the metallic canister, and the low permeability, plasticity capacity of this mineral can seal any fracture or deformations that could occur in the adjacent barriers.

The chemical composition of the interstitial water, and also the mineralogy composition of the bentonite, provides it geochemical stability and regulatory capacity against acid waters that could favor the corrosion of metallic elements of the canister, or alkaline waters that might come from the concrete barrier degradation.

Svensson et al. (2007) have selected the most proper bentonites to be used a barrier in the DGR facilities. All of them exhibit a montmorillonite content higher than 80%. In Spain, has been selected the FEBEX bentonite, with a montmorillonite content of $92\pm3\%$ in weight (Fernández, 2011).

2.6 Cementitious Water and its effect in nuclear spent fuel repositories

As it is described in previous sections, DRG consists in the interposition of natural and artificial barriers, between these nuclear wastes and the environment to isolate them until its radioactive activity decay to inoffensive levels.

Since cement is used in the clay barrier to contain nuclear waste and also as a sealing material, it is important to assess the effect of cementitious waters in contact with the spent fuel, because these materials might play an important role as physical and chemical barriers to the release of radionuclides into the far field. Therefore, the knowledge of long-term diffusion and adsorption properties of concrete and mortar is essential (Rojo et al. 2014). Large amounts of hydrated cement will determine the chemical and physical properties of the repository near-field for a long period of time (Berner, 1992).

Hydrated cement is largely defined by a system containing CaO, SiO_2 and water among other compounds (Berner, 1992) as it is shown in Table 4. The repositories for low and intermediate level radioactive wastes will include large quantities of cement waste matrices, construction elements and backfill materials.

Table 3. Proposed composition of backfilling mortar for use in containers (Gens, 2008)

Component	Content (kg/m^3)	Content (weight %)
CEM III/C 32.5 LA HSR LH	510	23,3
Silica fume	52	2.4
Calcareous aggregates (0/4)	1392	63,7
Water	223	10,2
Water/cement ratio	0,437	
Superplasticiser (Rheobuild 1100 conc. 30%, NS[b] type)	8,9 maximum[a]	0,406

[a] Could be adjusted downwards, depending on seasonal conditions

[b] Naphtalene sulphonate

As we can see at the table 4 due to the presence of silicate and calcium ions, most of the components in hydrated cement can cause the increase of the pH of waters in contact with it (Berner, 1992). Santos et al. (2006) studied the influence of pH on the corrosion

of SIMFUEL, an analogue of the SNF. The following oxidation mechanism at high pH was proposed:

$$UO_2 + xH_2O \rightarrow U_{1-2x}^{IV}U_{2x}^{V}O_{2+x} + 2xH^+ + 2xe^- \qquad \text{(eq. 1)}$$

$$U_{1-2x}^{IV}U_{2x}^{V}O_{2+x} + 3OH^- \rightarrow U^{VI}O_{2+x}(OH)_3^- + 2e^- \qquad \text{(eq. 2)}$$
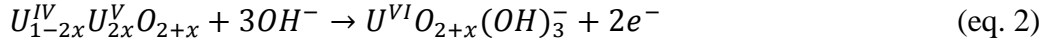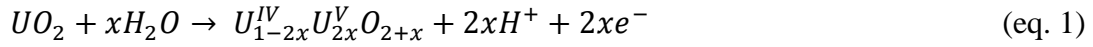
The physical and chemical properties of deposits formed on fuel surfaces will be determined by the combination of redox conditions, temperature and groundwater composition. Buck et al. (1998), Santos et al. (2006) showed that a complicated range of phases is possible as redox conditions evolve from oxidizing to eventually anoxic. The incorporation of calcium and the formation of silicates are a common feature of these phases, indicating that these groundwater constituents could exert an important influence on fuel corrosion over long periods of time (Santos et al. 2006).

In many cases, the cement is used for stabilizing contaminated wastes. This technique is one of the most popular solidification/stabilization (S/S) techniques prior to near-surface or underground disposal. Mixing radioactive waste products with a cementitious binder system improves the stabilization and the solidification of waste materials (Harfouche et al. 2006).

As we said previously, cement is used to condition the waste material and to construct the engineer barrier systems of the repository; more than 70 wt. % of the disposal galleries consists of cementitious backfill materials (Nagra, 2002).

Because of this, in the following sections, we're going to describe the effect of the calcium and silicate in the cementitious backfill materials when it gets in contact with the nuclear waste.

2.6.1 The effect of Calcium present in cement barriers for nuclear waste

Santos et al. (2006c) studied the effect of calcium presence. The study suggests that Ca^{2+} does not influence the surface oxidation process $UO_2 + xH_2O \rightarrow U_{1-2x}^{IV} + U_{2x}^{V}O_{2+x} + 2xH^+2xe^-$, but impede the subsequent formation of surface U^{VI} species which are thought to form via dissolution as UO_2^{2+}-deposition as $UO_3 \cdot yH_2O$ process.

The authors suggest that two possible explanations exist by which calcium adsorption could suppress the formation of U^{VI} surfaces species: blocking the O^{2-} anion transfer

reaction from the fuel surface or the adsorption of Ca^{2+} on the UO_2 surface that could impede the fuel dissolution.

2.6.2 The effect of Silicate present in cement barriers for nuclear waste

Santos et al. (2006b) also studied the effect of silicate; the electrodes used in this study were natural UO_2 doped with non-radioactive elements to replicate the chemical effects of CANDU reactor, and were anodically oxidized in a solution containing 0,1 M $NaSiO_3$ and 0,1 M NaCl at pH=9,5.

Santos et al. (2006b) concluded that the presence of silicate has little influence on the oxidation of UO_2 to produce an oxidized surface layer $U^{IV}_{1-2x}U^{V}_{2x}O_{2+x}$, nevertheless the silicate does not impede its formation. Due to the accumulation of U^{IV} on the $U^{IV}_{1-2x}U^{V}_{2x}O_{2+x}$ surface there is an increasing dominance of U^{VI} at higher potentials. Also, the study suggests the conversion of $U^{IV}_{1-2x}U^{V}_{2x}O_{2+x} \rightarrow UO_3 \cdot yH_2O$ is inhibited initially in silicate solution, possibly due to the adsorption of silicate on the fuel surface since the precipitation of a uranium-silicate hydrated phase was observed at high corrosion potentials (Shoesmith, 2007).

2.6.3 The effect of Calcium and Silicate present in cement barriers for nuclear waste

Groundwater might contain calcium and silicate which could lead to the formation of corrosion product deposits and the formation of insoluble U^{VI} phases (Shoesmith, 2007).

Harfouche et al., (2006) studied the uptake of U(VI) by calcium silicate hydrates (C-H-S) using X-ray absorption fine structure spectroscopy, for that C-H-S phases were synthesized using two different procedures: one based on the mixing of CaO and SiO_2 solids, and the other one is based on starting solutions of Ca and Si. The authors reported that some similarities exist between the experimentally determined structural parameters for U(VI)-doped with calcium silicate hydrates (C-S-H) and the structural parameters for uranophane: a structural model for U(VI) uptake by C-S-H phases.

Kienzler et al., 2006 studied the effects of the NaCl and $MgCl_2$ dissolutions in contact with a cement monoliths doped with U(VI), they found that the dominant uranium phase was uranophane in the corroded cement. Nevertheless, other possible uranium phases could precipitate such as soddyite, metaschoepite and di-uranate.

2.7 Main Uranium Health Effects

The study of the alteration process of the UO_2 helps to understand the behavior of the SNF matrix, which has more than 90% of the radionuclides. If due to corrosion process, the uranium is released to the groundwater, the contained radionuclides in the SFN matrix will be released.

This released radionuclides can contaminate water bodies, in consequence, the water that we ingest and cause major health problems.

The importance of controlling the waters that have been in contact with uranium is that the more water-soluble compounds present, the highest toxicity in human health (Keith et al., 2013).

When a contaminant is released from a large area such as an industrial plant or from a container such as drum or bottle, it enters the environment. But such a release does not always lead to exposure. Normally a person is exposed to a contaminant when he is in contact with it. That contact and/or exposure can occur when a person breathes, eats, drinks or touches that contaminant. However, since uranium is radioactive, someone can also be exposed to its radiation.

Even if is this person is exposed to uranium, he or she might be not harmed. Whether the person is harmed will depend on such factors as the dose (how much), the duration (time of the exposure), and how the person happens to contact it. Harm might also depend on whether the person has been exposed to any other chemicals or radioactive materials, as well as age, sex, diet, family, traits, lifestyle, and state of health.

Uranium's main target is the kidneys. Kidney damage has been in humans and animals after inhaling or ingesting uranium compounds. Ingesting water-soluble uranium compounds will result in kidney effects at lower doses than following exposure to insoluble uranium compounds. Once the uranium is in the bloodstream, the compounds are filtered by the kidneys, where they can cause damage to the kidney cells. Very high uranium intakes (ranging from about 50 to 150 mg depending on the individual) can cause acute kidney failure and death. At lower intake levels (around 25 to 40 mg), damage can be detected by the presence of protein and dead cells in the urine, but there are no other symptoms.

Renal effects have been observed in animals exposed to aerosols of soluble uranium compounds at concentrations superiors of 0,13 mg U/m^3 for intermediate durations. However, no renal effects were observed in animals exposed to 1,0 mg U/m^3 as insoluble compounds, the LOAEL (lowest-observed-adverse-effect level) was 8,2 m U/m^3 (Keith et al., 2013). These data suggest that soluble compounds are at least five times more toxic than insoluble compounds, as we said at the beginning of this text.

The available data on the oral and dermal toxicity of uranium are more limited than by the inhalation route. The available studies suggest that inhalation and oral exposure to low levels of uranium (doses or concentrations resulting in minimal renal effects), toxicity is not strongly influenced by the duration of exposure (Keith at al., 2013)

Some studies have examined the toxicity of depleted uranium in a small number of animals. These studies focused on renal toxicity and neurotoxicity. As with exposure to natural uranium, alterations in renal function and histopathology (swollen glomeruli, necrosis and fibrosis) were observed in rats exposed to depleted uranium. Acute exposure to depleted uranyl acetate in drinking water resulted in increased motor activity in male rats exposed to 28 mg U/Kg/day and female mice exposed to 6 mg U/kg/day. Implantation of depleted uranium pellets in rats resulted in measureable uranium in the brain at 6-18 months after the implantation, showing the bioaccumulation of the uranium, at least in animals; and, this accumulation was accompanied by electrophysiological changes in brain.

3. Analytical Methods

3.1 Scanning electron microscopy (SEM)

The scanning electron microscope permits the observation and characterization of heterogeneous organic and inorganic materials on nanometer (nm) to micrometer (μm) scale. The SEM has the capability of obtaining three-dimensional-like images of the surfaces of a very wide very wide range of materials (Goldstein et al. 2003). The major use is to obtain topographic images in the magnification range 10-1000X.

The scanning electron microscope (SEM) uses focused beam of high-energy electrons to generate a variety of signals at the surface of solid specimens. The signals that derive from electron-sample interactions reveal information about the sample including external morphology (texture), chemical composition, and crystalline structure and orientation of materials (Swapp, 2017). In most applications, data are collected over a selected area of the surface of the sample, and a 2-dimensional image is generated that displays spatial variations in these properties. Areas ranging from approximately 1 cm to 5 microns in width can be imaged in a scanning mode using conventional SEM techniques (magnification ranging from 20X to approximately 30,000X, spatial resolution of 50 to 100 nm). The SEM is also capable of performing analyses of selected point locations on the sample; this approach is especially useful in qualitatively or semi-quantitatively determining chemical compositions (using EDS), crystalline structure, and crystal orientations (using EBSD) (Swapp, 2017).

3.1.1 Operating Principle of the SEM

The electron source used in the SEM can be tungsten filament, else a LaB_6 or Schottky emitter, or a tungsten field-emission tip. Axially-symmetric magnetic lenses are used but they are also smaller than those employed in the TEM, for electrons of lower kinetic energy, the pole pieces need not generate such a strong magnetic field.
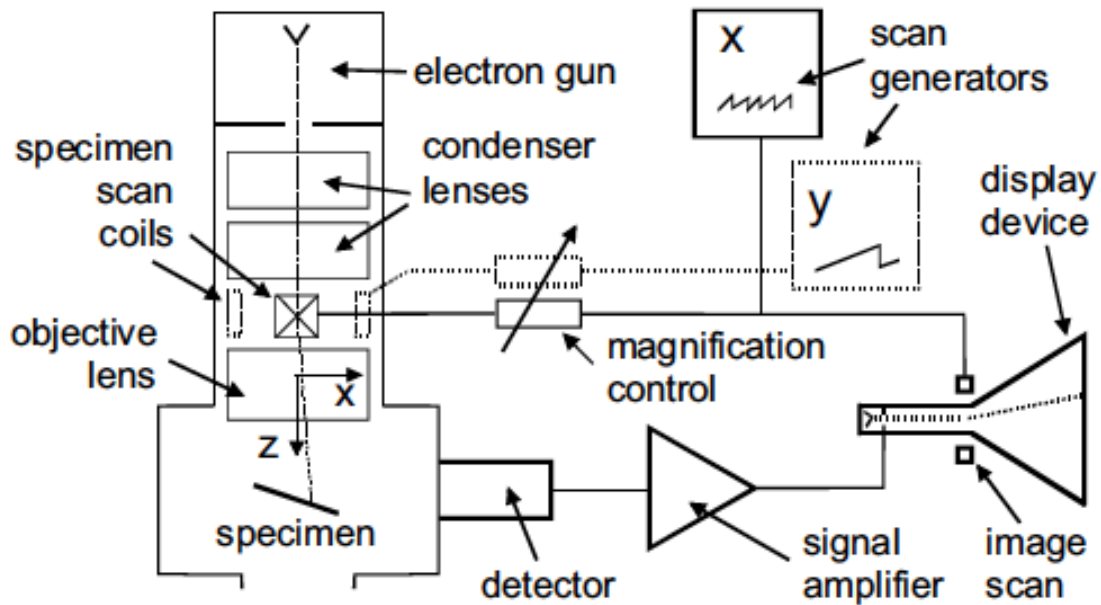
Figure 5. Schematic diagram of a SEM with a CRT display. Egerton, 2005

Figure 5, shows that there are usually two or three lenses, which act like the condenser lenses of a TEM. The incident beam in the SEM (also known as the electron probe) need to be as small as possible: a diameter of 10 nm is typical and 1 nm is possible with a field-emission source. The final lens that forms this very small probe is named the objective, its performance (including aberrations) largely determines the spatial resolution of the instrument, as does the objective of a TEM or a light-optical microscope. In fact, the resolution of an SEM can never be better than its incident-probe diameter (Egerton, 2005).

Whereas the conventional TEM uses stationary incident beam, the electron probe of a SEM is scanned horizontally across the specimen in two perpendicular (*x* and *y*) directions. The *x*-scan is relatively fast and is generated by a sawtooth-wave generator operating at a line frequency f$_x$. This generator supplies scanning current to two coils, connected in series and located on either side of the optic axis, just above the objective lens. The coils generate a magnetic field in the *y*-direction, creating a force on an electron that deflects it in the *x*-direction. The *y*-scan is much slower and is generated by a second sawtooth-wave generator running at a frame frequency. The entire procedure is known as raster scanning and causes the beam sequentially to cover a rectangular area on the specimen (Egerton, 2005).

3.1.2 Applications

SEM is routinely used to generate high-resolution images of shapes of objects (SEI) and to show spatial variations in chemical compositions: 1) acquiring elemental maps or spot chemical analyses using EDS, 2) discrimination of phases based on mean atomic number (commonly related to relative density) using BSE, and 3) compositional maps based on differences in trace element "activitors" (typically transition metal and Rare Earth elements) using CL. SEM is also widely used to identify phases based on qualitative chemical analysis and/or crystalline structure. Precise measurement of very small features and objects down to 50 nm in size is also accomplished using SEM (Swapp, 2017).

To conclude, the information that we can obtained from a scanning electron microscopy inspection (SEM) is:

- Surface topography if low energy secondary electrons are collected.
- Atomic number or orientation information if higher energy backscattered electrons are used for imaging.
- Differentiation between surface roughness, porosity, granular deposits, stress-related gross microcracks.
- Observation of grain boundaries in unetched samples.
- Critical dimension measurements.
- Elemental analysis.

3.2 X-ray photoelectron spectroscopy (XPS)

X-ray photoelectron spectroscopy (XPS) is applied to a wide range of materials, in order to obtain a variety of analytical information. Although XPS can be applied to gases, liquids and solids. XPS is essentially a large area analysis (some mm^2) with a characteristic analysis depth of several nanometers. The main objective of the XPS is the characterization of the surface or near surface regions of materials applied in areas of materials science such as adhesion, polymer chemistry, corrosion and composite materials (Watts, 1994).

XPS technique probes the energy distribution of electrons ejected from solids via irradiation by X-rays and the photoelectric effect; the electrons contain information regarding chemical oxidation state, electronic structure, and atomic composition the analyte studied. Thus, surface composition as well as the electronic environment can nondestructively be determined. X-ray photoelectron spectroscopy is also useful for quantitative analysis, capable of probing ultrathin layers of material. Since the photoelectrons analyzed come only from the topmost atomic layers of the solid surface studied ($\leq$100 Armstrong), the technique is an invaluable tool for studying interfacial phenomena at the solid-solid and solid-gas boundaries (Chusuei and Goodman, 2002).

3.2.1 The principles of XPS

A surface is irradiated with X-rays (commonly Al Kα or Mg Kα) in vacuum. When an x-ray photon hits and transfers this energy to a core-level electron, it is emitted from its initial state with a kinetic energy dependent on the incident X-ray and biding energy of the atomic orbital from which it originated. The energy and intensity of the emitted photoelectrons are analyzed to identify and determine the concentrations of the elements present in the sample; a photoelectron spectrum is recorded, as figure 10 shows, by counting ejected electrons over a range of electron kinetic energies. Peaks appear in the spectrum from atoms emitting electrons of a characteristic energy. The energies and intensities of the photoelectron peaks enable identification and quantification of all surface elements, except hydrogen. These photoelectrons originate from a depth of <10 nm therefore the information obtained is from within this depth (NPL, 2012)

As conclusion, the X-ray photoelectron spectroscopy is used for:
- Depth profiling on surfaces.
- Identification and measurement of surface contamination and organic over layers e.g. to solve problems of adhesion of coatings on substrates.
- Analysis of nanoparticles.
- Silicon dioxide on silicon thickness measurement for the semiconductor industry.
- Identification of counterfeit products.
- Catalysis and corrosion studies.

- Characterization of a wide range of materials such as paints, polymers, ceramics and glasses.

3.3 Raman spectroscopy

Raman spectroscopy (RS) resolves most of limitations of other spectroscopic techniques and can be used for both qualitative and quantitative purpose. Qualitative analysis can be performed by measuring the frequency of scattered radiations while quantitative analysis can be performed by measuring the intensity of scattered radiations (Bumbrah and Sharma, 2015).

3.3.1 The principles of Raman Spectroscopy

Raman spectroscopy, as said in the previous paragraph, is a scattering technique. It is based on Raman Effect: inelastic scattering of incident radiation through its interaction with vibrating molecules (Settle, 1997) (Chalmers et al, 2012).

The sample is illuminated with a monochromatic laser beam which interacts with the molecules of sample and originates a scattered light. The difference in frequency between the scattered light and the incident light is used to create a Raman spectrum. Raman spectra arise due to inelastic collision between incident monochromatic radiation and molecules of sample. When a monochromatic radiation strikes at sample, it scatters in all directions after its interaction with sample molecules (Bumbrah and Sharma, 2015). A small fraction of scattered radiation has a frequency different from frequency of incident radiation and this constitutes Raman scattering. When the frequency of incident radiation is higher than frequency of scattered radiation, Stokes lines appear in Raman spectrum. But when the frequency of incident radiation is lower than frequency of scattered radiation, anti-Stokes lines appear in Raman spectrum. Scattered radiation is usually measured at right angle to incident radiation (Skoog et al. 2007) (Willard et al. 1988).

A Raman spectrum is presented as an intensity-versus-wavelength shift. Raman spectra can be recorded over a range of 4000-10 cm^{-1}. Depending on spectrophotometer's design and optical components, typical Raman spectra cover the wavenumber region between 400-5 Δcm^{-1} and 4000-400 Δcm^{-1} (Bumbrah and Sharma, 2015).

The Raman spectrometers consist of: one or more single colored light sources (light), lenses: both to focus the light onto the sample and to collect the scattered light; filters to purify the reflected and scattered light so only the Raman light is collected; a means of splitting the light into its constituent colors (typically a diffraction grating or prism); a very sensitive detector to detect the weak light and a device such as a computer to control the whole system which displays the spectrum and enables the information so the sample can be characterized.

Raman spectrophotometers can be dispersive or non-dispersive. Dispersive Raman spectrophotometer uses an interferometer use prims or grating while non-dispersive Raman spectrophotometer uses an interferometer such as Michelson interferometer in Fourier Transform Raman spectrophotometer.

Normally, laser sources are used and provide stable and intense beam of radiation. Wide range of lasers such as Argon ion laser (488 and 514,5 nm), Krypton ion laser (530,9 and 647,1 nm), Helium-Neon (He-Ne) (632,8 nm), Near Infrared (IR) diode lasers (785 and 830 nm), Neodymiun-Ytrium Aluminum Garnet (Nd:YAG) can be used as light source in Raman spectrophotometers. Short wavelength sources such as argon ion and krypton ion lasers can produce significant fluorescence and cause photodecomposition of the sample (Bumbrah and Sharma, 2015).

In Raman microspectroscopy, Raman spectrophotometer is interfaced to an optical microscope which enables both visual and spectroscopic examinations as either as single point, mapping or imaging measurements. Microscope is used to focus the laser beam onto the sample. Raman microspectrophotometry enables the visual inspection of sample and facilities spectroscopic analysis of a limited amount of sample or a selected small region within a sample (Bumbrah and Sharma, 2015).

Raman spectrophotometers can be categorized in two broad classes, depending on the area of use: lab based spectrophotometers and in-field, in situ or down-field use Raman spectrophotometers. The basic principle is same in each case and these systems are differentiated by versatility of an instrument and size and relative cost of its components. In this case was used a stand-off Raman spectrophotometer which are available for on-site analysis and research purpose (Bumbrah and Sharma, 2015).

4. Experimental Methodology

4.1 Electrochemical instrumentation

Electroanalytical chemistry encompasses a group of quantitative analytical methods that are based upon the electrical properties of an analyte solution when it is made part of a cell. There are two general types of electrochemical methods: potentiometric (no current, equilibrium potential) and voltammetric where current is measured as a function of the applied potential.

An electrochemical cell consists of two electrodes: an anode, at which the oxidation reaction occurs, and the cathode, the electrode at which the reduction reaction occurs. The electrodes transport produced electrons from one half-cell to another, which produce an electrical charge. In an electrochemical cell, we might find three types of electrodes:

- *Working electrode*: the electrode at which the reaction of interest occurs.
- *Counter electrode*: the electrode, at which the other (coupled) reaction occurs.
- *Reference electrode*: an electrode that has an established electrode potential.

Finally, a solution is used as electrolyte, which allows the electron transfer between the working electrode and the counter electrode. Additionally, it usually contains ions with either positive or negative electrical charge.

4.1.1 The Cell

A Metrohm glass vessel of 50 ml (fig. 7) was used for the electrochemical measurements. The dropsens electrode was connected through the USB connection (DRP-CAC 71569) to the Metrohm Autolab Potentiostat-Galvanostat M204, and was controlled by using the NOVA software 2.1 version.

With the Metrohm Autolab Potentiostat-Galvanostat we can perform measurements in potentiostatic or galvanostatic mode. In the specific case of potentiostatic mode, experiments are done at a fixed DC potential. A sinusoidal potential perturbation is superimposed on the DC potential and applied to the cell; the resulting current versus time is measured in this type of experiments.

The Dropsens electrodes were used as counter, working and reference electrode, their characteristics are shown in following sections.
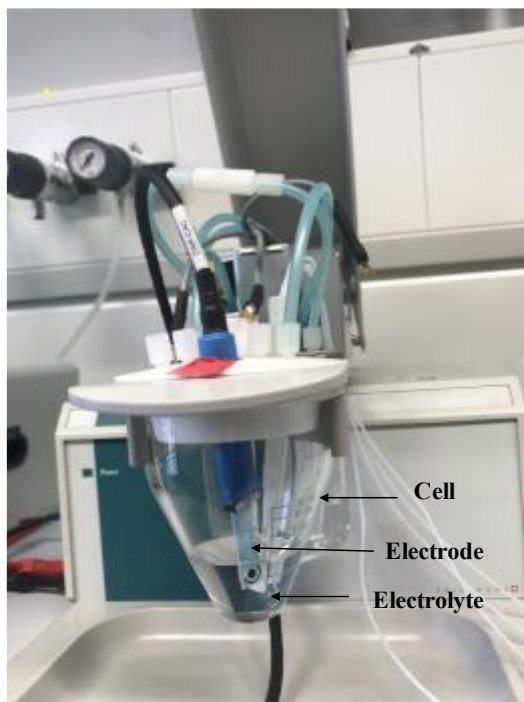
Figure 6. The cell used to perform all the experiments.

4.1.2 The Electrolytes

Three types of electrolyte were used to perform the electrochemical analyses.

The solutions were prepared using AppliChen Panreac, Fluka, Merck and Scharlau chemicals. Milli-Q water 18,2 MΩ. cm at 25ºC generated by a Millipore water purification system was used for the preparation of the solutions.

First, a Na^+Cl^- 0,1 M pH=12 solution was used. This first solution worked as blank.

Then, a Na^+Cl^- 0,1 M, SiO_3^{-2} 0,001M pH=12 solution was used as second electrolyte, and finally a Na^+Cl^- 0,1 M, SiO_3^{-2} 0,001M and Ca^{2+} 0,0001 M pH=12 was used as a third electrolyte. The pH was adjusted in all cases with a pH meter from Hanna instruments, model H12002-02 software version 1.08.

A Na^+OH^- solution 0,1 M was also used to adjust the pH when necessary.

These solutions were used to perform cyclo-voltammetric measurements and could determine if silicate and calcium have any effect on the UO_2 corrosion process.

Table 4. Summary of electrolytes used to perform electrochemical studies

	pH	First Electrolyte	Second Electrolyte	Third Electrolyte
Na⁺Cl⁻ (blank)	12	0,1 M	0,1 M	0,1 M
SiO₃⁻²	12	-	0,01 M	0,01 M
Ca²⁺	12	-	-	0,001 M

4.1.3 Dropsens Electrode

The Dropsens electrodes are screen-printed electrodes (SPEs) based on carbon, manufactured by Dropsens for electrochemical analysis in environmental, clinical or agri-food areas. They are disposable, low cost devices specially designed to work with micro volumes of sample or dip them in solutions.

The carbon SPEs characteristics are the following:

Table 5. Carbon SPEs (Dropsens) characteristics. Dropsens.com

Ceramic Substrate	L33xW10xH0.5 mm
Electric contacts	Silver
Electrochemical cell	--
Working electrode	Carbon 4 mm diameter
Auxiliary electrode	Carbon
Reference electrode	Silver

All potentials are specified or reported as the potential of the working electrode respect to the reference electrode, in this case was Ag/AgCl.

29

On the following image, it is possible to locate the reference, working and counter electrode on the surface of the carbon SPEs.
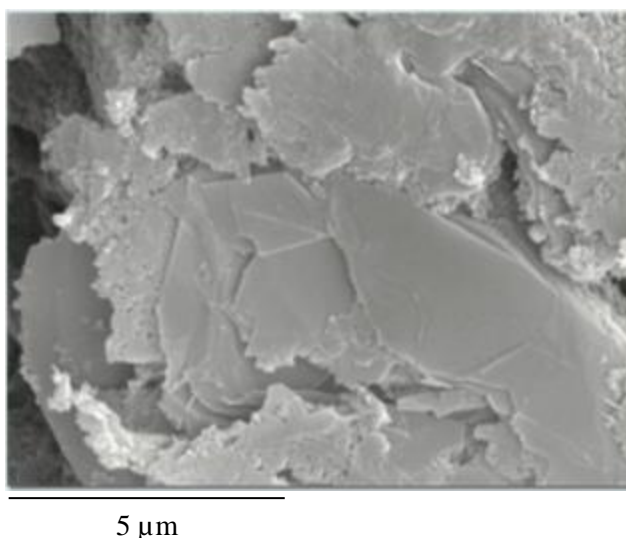

1	Counter Electrode
2	Working Electrode
3	Reference Electrode
a	C.E. connection
b	W.E. connection
c	R.E. connection
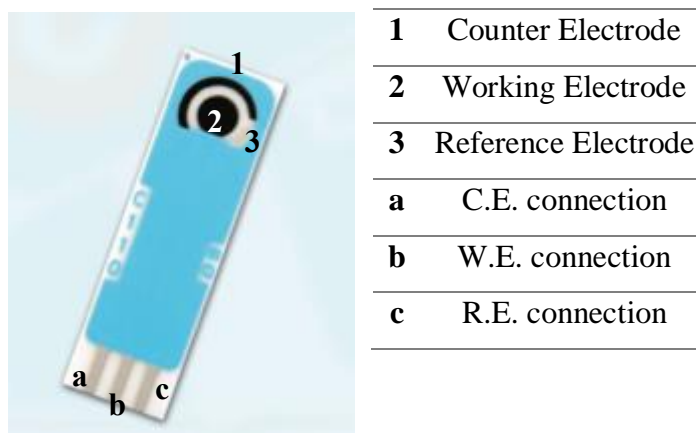
Figure 7. Dropsen used to perform
all the experiments.

The following photo (figure 8) shows a SEM image of the Dropsen before performing any experiment.

5 µm

Figure 8. SEM image of working electrode. Dropsens.com

It is important to remark that all the experiments were performed under environmental conditions, in contact with air. As a consequence, the oxygen concentration in solution remains constant. The oxygen is never totally consumed by the oxidation of the working electrode due to the oxygen diffusion from the atmosphere.

4.2 Dropsens surface modification: Deposition of UO$_2$

The UO$_2$ stripping was done by using the Autolab Potentiostat-Galvanostat M204, all the conditions used to perform the experiment were specified in the NOVA software 2.1 version. Two types of electrodes with UO$_2$ were prepared: one with deposition time of 15 minutes and another one with deposition time of 60 minutes.

The stripping procedure was performed using a dissolution of uranyl acetate with a concentration of 0,06 M and pH 4,5 (fig. 9). Once the procedure was done, the electrode was rinsed with sufficient Milli-Q water.


Figure 9. Deposition of UO$_2$ on dropsen electrode surface

4.2.1 SEM Images of deposited Dropsen® surface

After the electrodeposition, a characterization with XPS and Raman spectroscopy was performed to the modified electrodes.

The composition of the resulting surface of the electrode was characterized by SEM. The analisys observations were performed at Barcelona Research Center for multiscale science and engineering (BRCMSE), situated in UPC-Diagonal Besòs.
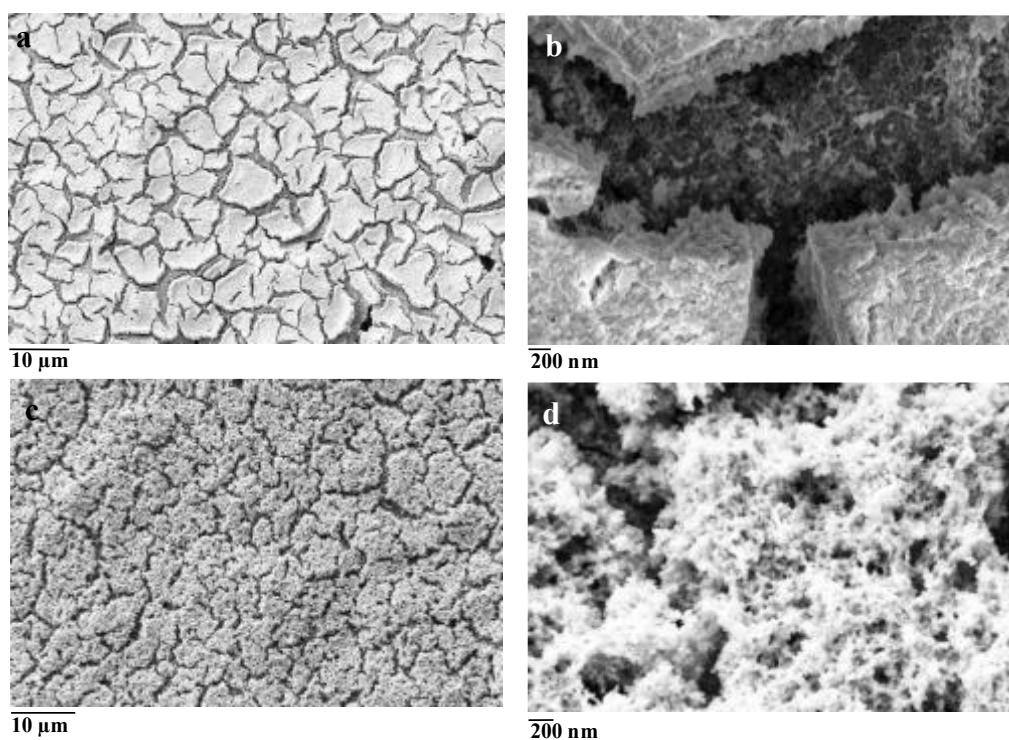
Figure 10. SEM images from deposited electrode. (a) 3.00K X 15-min deposition time, (b) 50.00K X 15-min deposition time, (c) 3.00K X 60-min deposition time, (d) 50.00K X 60-min deposition time

The figure 10a shows a SEM image with a 3.00K X magnitude, of the surface of the screen-printed electrode (Dropsens). As this image shows, the Dropsens surface was substantially modified by the deposition of a solid phase.

The precipitate obtained has been deposited on the different layers that makes up the carbon electrode surface, it will explain the presence of the fractures that are observed in the image.

In figure 10b, it is possible to observe a SEM image with a 50.00K X magnitude, corresponding at the same surface electrode deposited with UO_2.

The SEM photograph shows with much clarity the fractures, also it is possible to observe the porosity of fractures edges.

Following, the figure 10c shows a SEM image with 3.00K X magnitude of the screen-printed electrode surface. This electrode has been deposited with UO_2 for 60 minutes.

It is possible to observe the fractures that also appear in the fig. 10a and 10b, but the layer deposited in the surface electrode for 60 minutes appears to be more porous than that deposited for 15 minutes'.

The figure 1d shows a SEM image with a 50.00K X magnitude of the 60 minutes deposited electrode. It is possible to observe with more detail the porosity of the surface, this SEM image confirm the information that is shown in the figure 11c.

4.2.2 Raman spectroscopy of deposited Dropsen® surface

Raman microspectrometric measurements were carried out with a Renishaw confocal inVia Qontor Raman spectrometer (Renishaw PLC., England).

Raman backscattering was excited with a 535-nm excitation wavelength. Individual spectra were obtained using an exposure of 10 s over the wavenumber range from 1100 to 2250 cm^{-1} for carbon and from 0 to 1150 cm^{-1} for UO_2. The laser was focused onto the sample using a 20X uncoated-objective lenses at the Dropsens electrode.
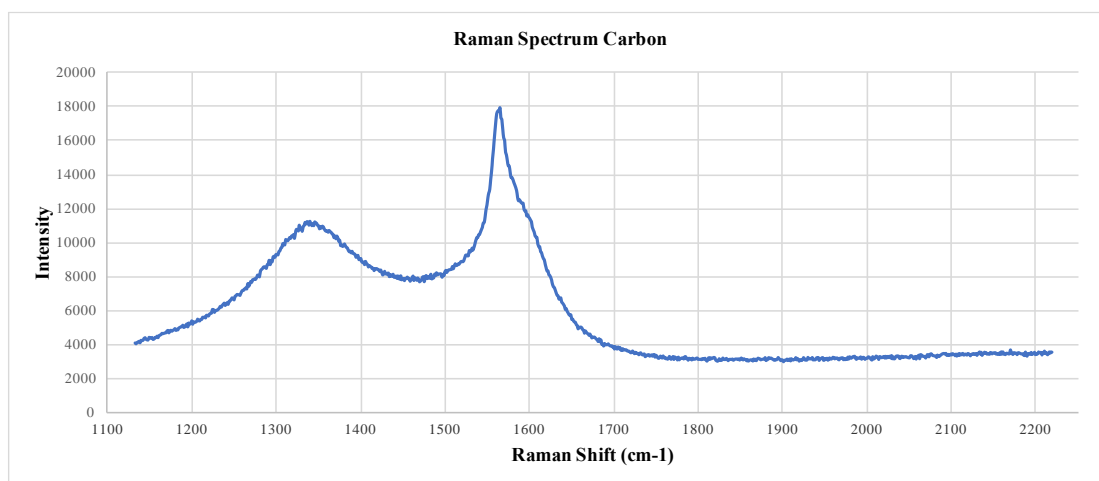
Figure 11. Raman spectrum for the electrode with no deposition

The Raman spectrum shown in the figure 11 corresponds to the dropsens with no deposition. As specified in section 4.1.3, the screen-printed electrode was based in carbon, hence the graphic shows the spectrum corresponding to the carbon at 1562 cm^{-1}. This information is corroborated by the bibliography, locating the carbon materials bands in the Raman spectra, between 1300 and 1700 cm^{-1} (Escribano et al. 2001) (Wang et al. 1990).

Figure 12 shows the Raman spectra carried out in the modified electrode.
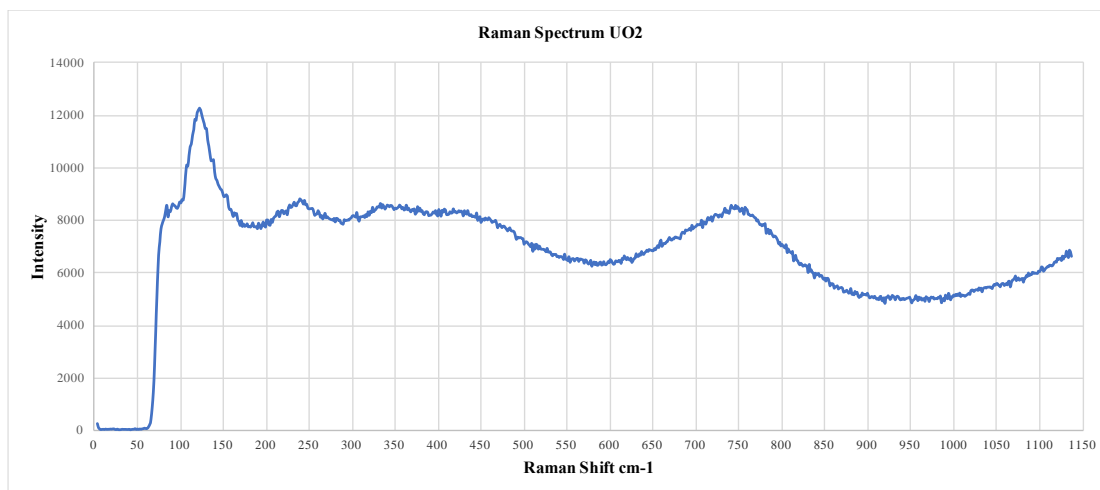
Figure 12. Raman spectrum for the electrode with deposition of UO_2

The characteristic Raman spectra for uranium oxides phases reported in the bibliography are collected in table 6.

If we compare the values shows in the table 6 and the Raman spectrum in the figure 12, it is possible to observe that the peaks doesn't appear at any values according to the bibliography. Nevertheless, the most closer Raman shift to that one obtained in the experiment, is the orthorhombic structure (U_3O_8) with a Raman shift value of 412 cm^{-1} and 738 cm^{-1} (table 6).

Table 6. Summary of Raman spectrum assignation for the uranium oxides (Elorrieta et al. 2017)

Crystallographic System	Raman actives modes	Raman shift (cm^{-1})	Raman spectrum	Reference
Cubic (Fluorite structure) (UO_2; U_4O_9)	T_{2g}	445	U-O	He and Shoesmith, 2010
		1150	2L-O	
Tetragonal (U_3O_7)	$A_{1g}+2B_{1g}+3E_{g}$	155	B_{1g}	
		255	E_g	
		315	B_{1g}	
		402	E_g	
		470	E_g	
		630	A_{1g}	
Orthorhombic (U_3O_8)	---	343	U-O	Manara and Renker

		412	U-O	
		483	U-O	
		738	O-U-O-U	
		811	U-O	

4.3 Electrochemical Measurements

4.3.1 Cyclic Voltammetry

Cyclic voltammetry (CV) is an electrochemical technique which measures the current that develops in an electrochemical cell under conditions while the potential applied between the working electrode and the reference electrode changes with time.

A cyclic voltammogram is obtained by measuring the current at the working electrode during the potential scans (Kissinger and Heineman, 1983). The following figure shows a cyclic voltammogram resulting from a single electron reduction and oxidation considering the following reversible reaction:
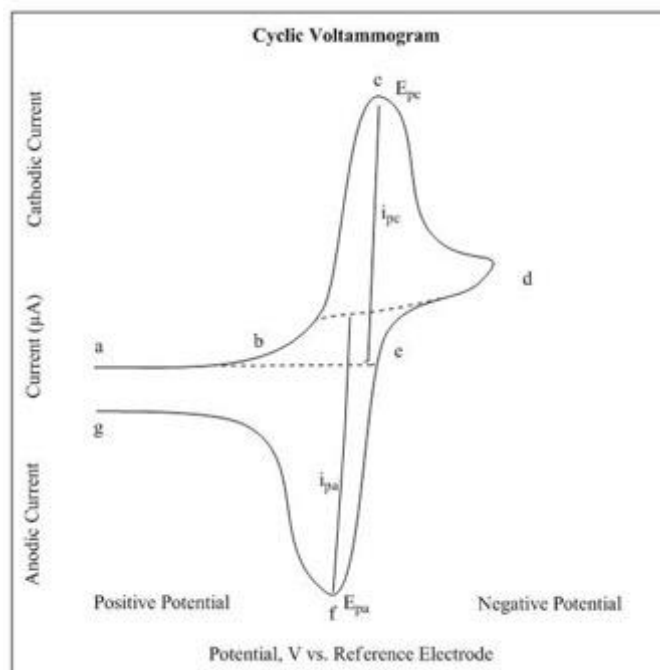
$$M^+ + e^- \leftrightarrow M \qquad\qquad (eq.\ 3)$$

Figure 13. CV of a single electron oxidation-reduction. Quiroga, 2017

In fig. 13, the reduction process occurs from the initial potential (point a) to the switching potential (point d). In this region, the potential is scanned negatively to cause a reduction. The resulting current is called cathodic current (i_{pc}). The corresponding peak potential occurs at the point c, and is called the cathodic peak potential (E_{pc}). The E_{pc} is reached when all the substrate at the surface of the electrode has been reduced. After the switching potential has been reached (point d), the potential scans positively from point d to point g. This results in anodic current (I_{pa}) and oxidation to occur (Skoog et al. 2007). The peak potential at point f is called the anodic peak potential (E_{pa}), and is reached when all the substrate at the surface of the electrode has been oxidized.
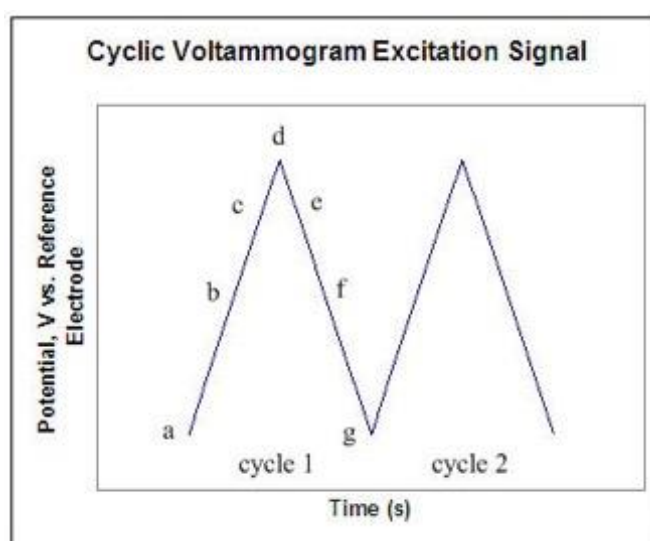
Figure 14. Cyclic Voltammogram Excitation Signal. Quiroga, 2017

As figure 14 shows, the potential first starts at negative values (reducing potentials) (point a) and it ends high positive potential (point d). The potential extrema (d) is call the switching potential, and is the point where the voltage is enough to have caused the oxidation of the analyte. The reverse scan occurs from the point d to the point g, where the potential is negative again, closing the potential cycle. Figure 17 shows a typical reduction occurring from the point d to point g and oxidation occurring from point a to point d (Quiroga, 2017).

In the following sections, all the electrochemical experiments are explained. Before to perform any experiment, the cell was washed, left overnight in a solution of HNO_3 5% to remove any ion that could affect the results, then was rinsed with Milli-Q water.

4.3.2 Cyclic-voltammetry experiments

Cyclic-voltammogram experiments were performed to study the behavior of the modified electrode in different types of electrolytes. The potential was scanned between -1,4 V to +0,7 V vs. Ag/AgCl saturated reference electrode, the scan rate used was 0,01 V/s. The CV runs were done under oxidizing atmosphere.

For each CV study performed, new initial solution was used and a careful cleaning of the cell to avoid the presence of ions that could affect the experiments and, as a consequence, alter the results.

4.3.3 Potentiostatic experiments

To determine the effect of the presence of each ion and the reactions involved in the corrosion process, potentiostatic experiments were performed. In this thesis, a potentiostatic experiment was perfomed at a fixed potential of 245 mv for each type of electrolyte (table 4). The electrode used in this case was the dropsen with a previous deposition time of 60 minutes. The experimental time was about 1 hour. A graphic of density current versus time was obtained.

4.3.4 Open circuit potential measurements

The open circuit potential, also referred to the corrosion potential, is defined as the potential between the cathodic and the anodic electrodes at their corrosion current density (Pérez, 2004). Experiments based on the measurement of the open circuit potential are potentiometric experiments.

Here, the current applied was 0 A between the 60 minutes' deposition electrode and the counter electrode for 24 hours. Then, the evolution of the potentials as a function of time was recorded. The electrolytes used are shown in table 4.

5. Results and Discussion

5.1 Cyclic-voltammetry results

5.1.1 Comparison between each electrolyte using electrode with no deposition

In fig. 15 a three set of cyclic-voltammogram recorded on the electrode with no deposition is detailed with each type of electrolyte: Na^+Cl^- 0,1 M pH=12; SiO_3^{-2} 0,001M pH=12 and SiO_3^{-2} 0,001M and Ca^{2+} 0,0001 M pH=12. The scan rate used was 0,01 V/s in each case, the studied region went from -1,4 V to 0,7 V.
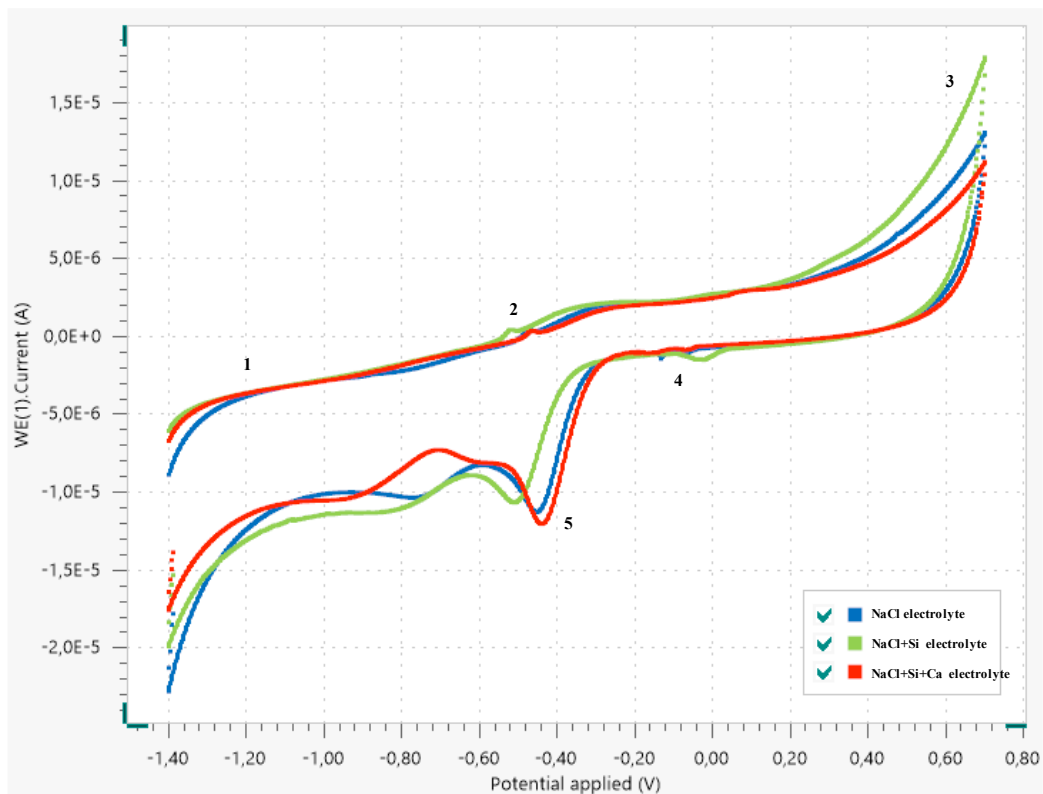
Figure 15. Cyclic voltammogram recorded on Dropsen with no deposition for Na^+Cl^- 0,1 M pH=12; SiO_3^{-2} 0,001M pH=12 and SiO_3^{-2} 0,001M Ca^{2+} 0,0001 M pH=12 electrolytes.

In Na^+Cl^- electrolyte, the current density increases following a linear tendency, as occur in the other two cases (SiO_3^{-2} and SiO_3^{-2}, Ca^{2+} dissolutions) (region 1).

One oxidation peak, on the anodic region, is observed: at 0,5 V for each electrolyte (region 2). The region 3 that occurs at the anodic limit of 0,7 V, the density current increase due to the limit conditions that produces the water oxidation.

The cyclic-voltammograms recorded in SiO_3^{-2} and Ca^{2+} electrolyte, are similar in the anodic section. As mentioned before, the peak is also observed at 0,7 V. The value

reached for current is very similar for both Na^+Cl^- and SiO_3^{-2} electrolyte $1,66\times10^{-5}$ and $1,79\times10^{-5}$ $A.cm^{-2}$ respectively; while the reached value for current for Ca^{2+} is lower than Na^+Cl^- and SiO_3^{-2} electrolyte around $1,12 \times10^{-5}$ $A.cm^{-2}$.

On the cathodic region, region 4 and 5, one reduction peak is observed at -0,05 V. The other reduction peak is observed at -0,46 V for Na^-Cl^+ and SiO_3^{-2}, Ca^{2+} electrolytes. For SiO_3^{-2}, the reduction peak is observed at -0,55 V.

In the following section a comparison was done between 15-min and 60-min deposition time of the modified electrode, in order to decide which electrode presented the most stable and reproducible behavior to perform the future experiments.

5.1.2 Comparison between 15-min and 60-min deposition modified electrode for Na^+Cl^- electrolyte
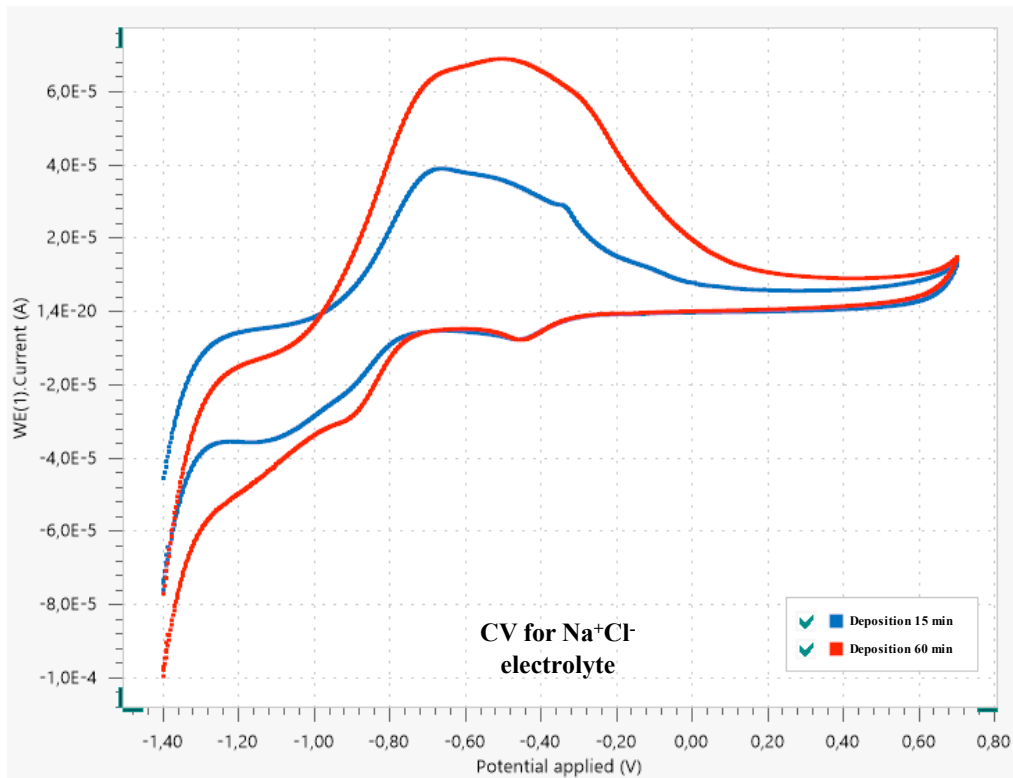
Figure 16. Comparison between the Dropsen electrode with no deposition, 15-min and 60-min deposition of UO_2 for the SiO_3^{-2} 0,001M pH=12 electrolyte.

Another comparison was done between the electrode with no deposition, 15 minutes' deposition and 60 minutes' deposition, to study the behavior of it for each electrolyte

and observe if it is any difference between them, according to the response in the dissolution.

In the figure 16, it is possible to observe the presence of an immense oxidation peak for the modified electrode, and there is no an important oxidation peak for the electrode with no deposition

As it is observed in the figure 16, for the 15 minutes' deposition time, an oxidation peak is observed from -0,15 V to -0,15 V, it reached a density current value of $4,0 \times 10^{-5}$ A.cm^{-2}. As the image shows, this peak is less large compared to 60-min deposition. For the 60 minutes' deposition time, also an important oxidation peak occurs from the -1,00 V to 0,15 V which reaches its maximum at -0,49 V corresponding to the $6,89 \times 10^{-5}$ A.cm^{-2} density current value.

On the cathodic region, one reduction peak is observed that occurs at -0,48 V. The behavior of the two modified electrodes is very similar.

The reverse scan shows a reduction peaks that correspond to the oxidation peaks occurring in the cathodic region of the cyclic-voltammogram.

The very large current at more negative potentials is to be due to the reduction of H_2O to H_2.

5.1.3 Comparison between 15-min and 60-min deposition modified electrode for SiO_3^{-2} electrolyte

In the following image (fig. 17), the behavior of the Dropsen with no deposition, 15 min and 60 min deposition time in the SiO_3^{-2} electrolyte was compared.

The cylic-voltamogramm for 60-min deposition time on the electrode presented two oxidation peaks: the first at -0,70 V and $1,40 \times 10^{-5}$ A.cm^{-2} value of current density and the second one at -0,57 V and $1,09 \times 10^{-6}$ A. cm^{-2}. At the anodic limit of 0,70 V a peak is observed due to the oxidation limit of the water.
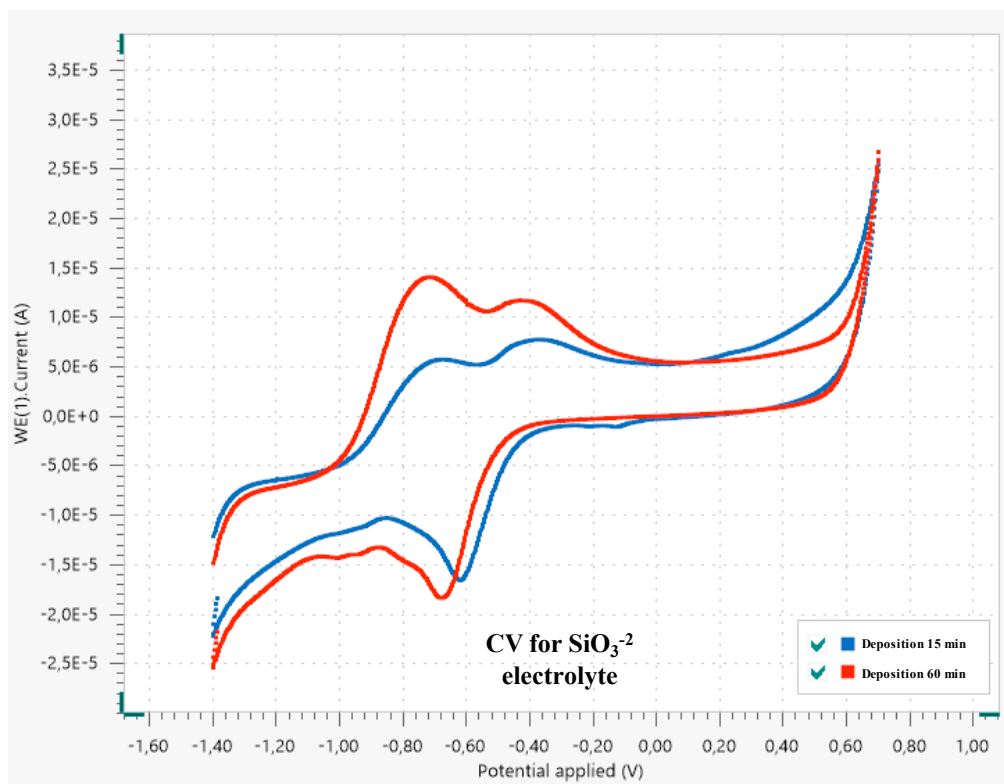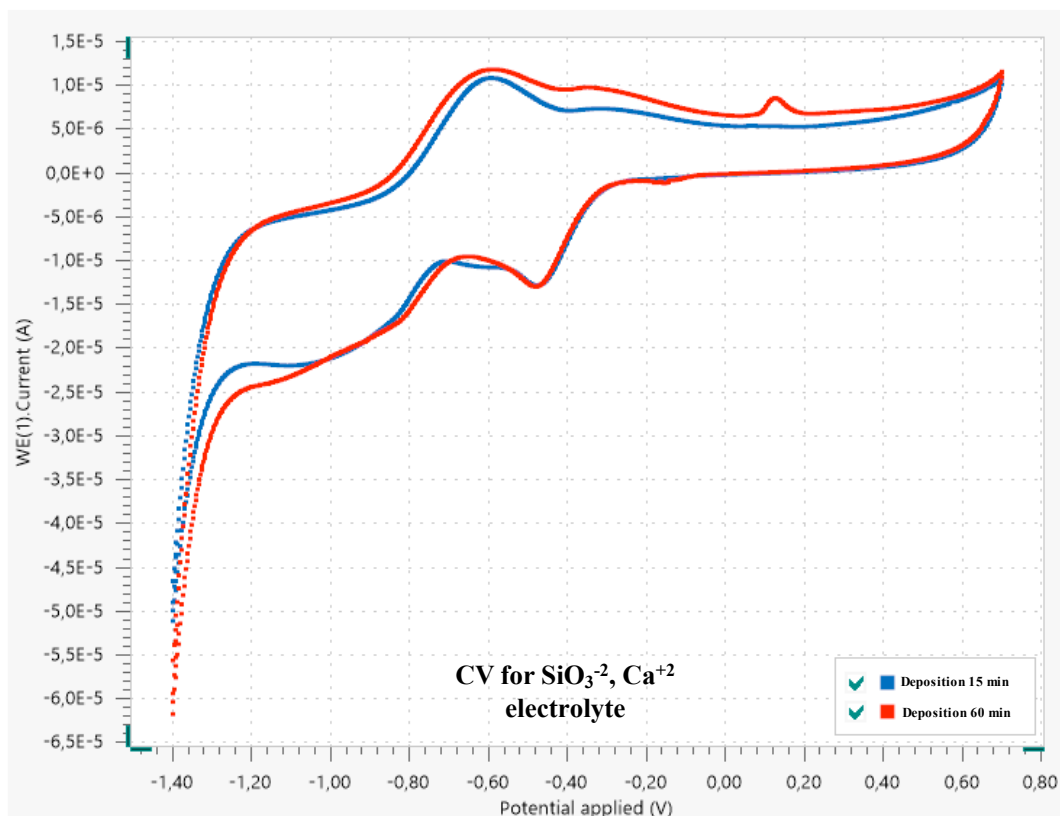
Figure 17. Comparison between the Dropsen electrode with 15-min and 60-min deposition time for the SiO 0,1 M pH=12 electrolyte.

As expected, based on the previous results, the cyclic-voltamogram for the electrode of 15-min shows the oxidation peaks in a voltage range similar to the 60-min deposition, but the density current shows lower values: $5,65 \times 10^{-5}$ A.cm^{-2} and $5,23 \times 10^{-5}$ A.cm^{-2} for each oxidation peak.

At the cathodic region, different reduction peaks are observed at more negatives potentials for 60-min compare to 15-min deposition time.

5.1.4 Comparison between 15-min and 60-min deposition modified electrode for SiO$_3^{-2}$, Ca^{2+} electrolyte.

The last comparison was done with the different deposited electrodes, using the SiO$_3^{-2}$, Ca^{2+} electrolyte, the cyclic-voltammograms are shown in the following image (fig. 18).

Figure 18. Comparison between the Dropsen electrode with 15-min and 60-min deposition time for the SiO$_3^{-2}$ 0,001M, Ca^{2+} 0,0001 M pH=12.

Regarding the electrode with 60-min deposition time, two oxidation peaks are observed. The first one occurs at -0,54 V, and the second one occurs at 0,14 V. As seen in previous cases, a peak is observed at the anodic limit of 0,7 V, where we are approaching to the water electrolysis.

The electrode with 15-min deposition time, shows a similar cyclic-voltammogram respect to the 60 min-deposition. Just one oxidation peak is observed at -0,60 V, approximately.

On the cathodic region, two reduction peaks are observed for both cases, the first peak appears at -0,50 V and the second one appears at -0,85 V.

After several tests, the electrode with 60-min deposition showed a more stable and reproducible behavior, in consequence, this modified electrode was used to perform the following experiments.

5.1.5 Comparison between each electrolyte using electrode with 60-min deposition time

A dropsen with deposition for 60 minutes was used to record a cyclic-voltammograms in Na^+Cl^- 0,1 M pH=12; SiO_3^{-2} 0,001M pH=12 and SiO_3^{-2} 0,001M, Ca^{2+} 0,0001 M pH=12 electrolytes. The behavior of the electrode for each electrolyte was compared in fig. 16.

5.1.5.1 Cyclic-voltammogram recorded for Na^+Cl^- electrolyte with electrode of 60-min deposition time.

In region 1, current density increases in almost linear tendency until region 2, where a grand oxidation peak is observed, between -1,00 V and 0,20 V, reaching a current density value of $6,9x10^{-5}$ A. cm^{-2}.

On the cathodic region, a reduction peak is observed in the reverse scan at approximately at -0,48 V.

*5.1.5.2 Cyclic-voltammogram recorded for SiO_3^{2-} electrolyte with electrode of 60-min deposition time.*

The cyclic-voltamogramm recorded using a SiO_3^{-2} electrolyte is shown (fig 16). In region 1, an increase of the current density is observed until region 2, where two oxidation peaks are shown, the first appears at -0,71 V and the second peak appears at -0,4 V reaching a current density value of $3,0x10^{-5}$ A.cm^{-2} and $1,17x10^{-5}$ A.cm^{-2}, respectively. On the cathodic region, one reduction peak is observed at -0,75 V.

5.1.2.3 Cyclic-voltammogram recorded for SiO_3^{2-}, Ca^{2+} electrolyte with electrode of 60-min deposition time.

On the anodic region, the density current increases until an oxidation peak is observed at -0,60 V (region 2). A second oxidation peak is observed at 0,13 V (region 3) with a density current value of $1,25x10^{-5}$ A.cm^{-2}.

On the cathodic region, two reduction peaks are observed, the first one occurs at -0,50 V and the second one occurs at -0,85 V, approximately.
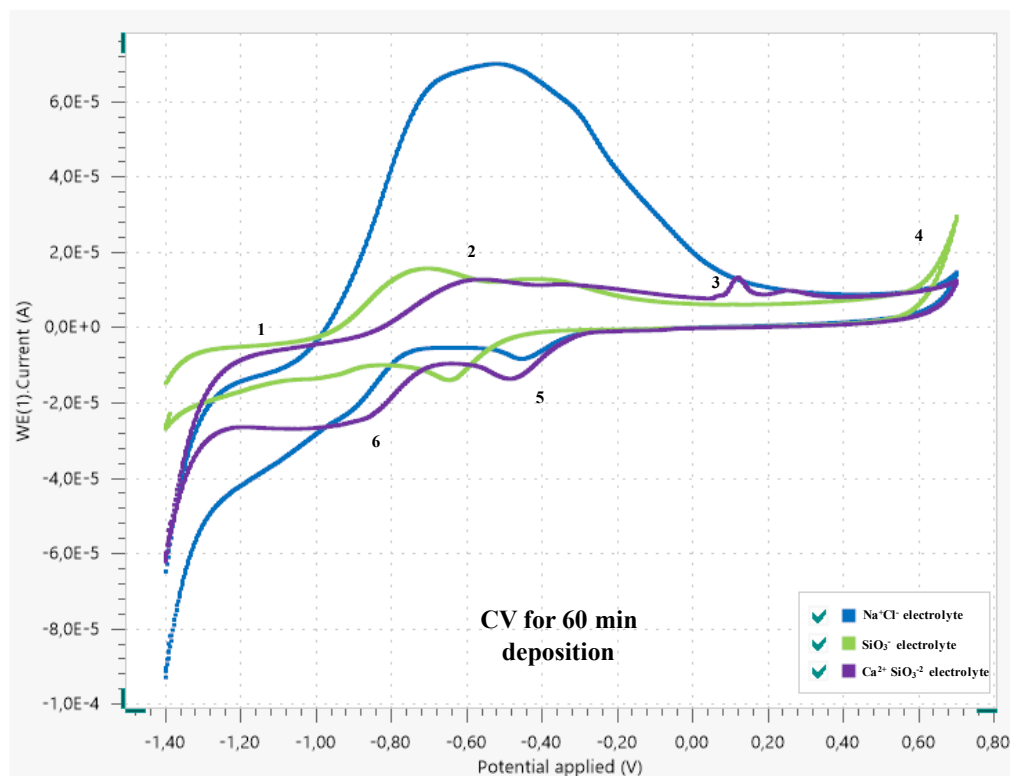
Figure 19. Cyclic voltammograms recorded on Dropsed with UO_2 60 minutes' deposition for Na^+Cl^- 0,1 M pH=12; SiO_3^{-2} 0,001M pH=12 and SiO_3^{-2} 0,001M Ca^{2+} 0,0001 M pH=12 electrolytes.

After the comparison of the electrode with 60-min deposition for each electrolyte was done, 6 regions were identified for the modified electrode behavior in each solution.

1.- Santos et al., (2006) recorded cyclic-voltamograms using SIMFUEL in a dissolution of NaCl 0,1 M at different pH values, including pH=13. They found a similar region, where the current was no significant. In their case, the potential range was wider than in our results because they used doped uranium. The presence of this region is due to the oxidation of non-stoichiometric UO_{2+x}.

2.- The presence of this peak might be due to the occurrence of several oxidation process, dissolution and/or precipitation of U^{VI}, probably concentrated at grain boundaries (Shoesmith, 2000). Nevertheless, more corrosion studies have to be done, to know what is happening in this region. As we can see in fig. 19, this process appears to be mitigated by the presence of the Si and Ca dissolutions. The Ca and Si act as agents that might be preventing the oxidation process.

Shoesmtih et al., (1989) studied solutions with high concentrations of dissolved oxygen. The authors showed that a film growth on UO_2 in two stages. The first stage is the relatively rapid formation of a UO_{2+x} surface layer, and the second stage of film growth occurs more slowly.

44

It appears that the SiO_3^{-2} dissolution provides the conditions to a more rapid oxidation and dissolution of these two layers.

3.- At 0,10 V, the SiO_3^{-2}, Ca^{2+} dissolution contributes to the dissolution and accumulation of protective corrosion products deposits (Shoesmith, 2000), such as soluble uranyl species, UO_2^{+2}, which have limited solubility at this pH (Grenthe et al., 1992) leading to the formation of a U^{VI} deposit (possibly $UO_3 \cdot yH_2O$) on the electrode surface (Santos et al. 2006), which is reinforced by the presence of the Ca and Si dissolutions.

4.- This region where potential is over 0,3 V, a rapid dissolution might be caused by the development of local acidity causing grain boundary etching and pitting (Shoesmith, 2000).

5.- The presence of the reduction peak might be due to the presence of impurities in our electrode with no deposition or the dissolutions. This conclusion is done, because this same peak is observed in the cyclic-voltammograms recorded using non-deposited electrodes. Nevertheless, tt is necessary to perform more electrochemical studies to know with more detail the process related to the apparition of this peak.

6.- On the reverse cathodic scan the $UO_3 \cdot yH_2O \rightarrow UO_{2+x}$ reduction process is observed, at the potential range from –0,80 V to -1,20 V. (Santos et al., 2006)

At more negative potentials, the reduction limit of wàter is observed.

5.2 Pontentiostatic results

The potentiostatic experiments were performed for the deposited electrode under the indicated conditions in section 4.3.3.

Figure 20 shows current density versus time. The highest current density was obtained for SiO_3^{-2} and Ca^{2+}, SiO_3^{-2}, an overlap of both cases can be observed. The lower current density was obtained for Na^+Cl^-.

This information is corresponding with that obtained in the cyclic-voltammogram, because as it is shown in the figure 20 for a potential of 245 mV, the lowest density current value is observed in the Na^+Cl^- electrolyte and the highest density current value are observed in SiO_3^{-2} and Ca^{2+}, SiO_3^{-2} dissolutions.
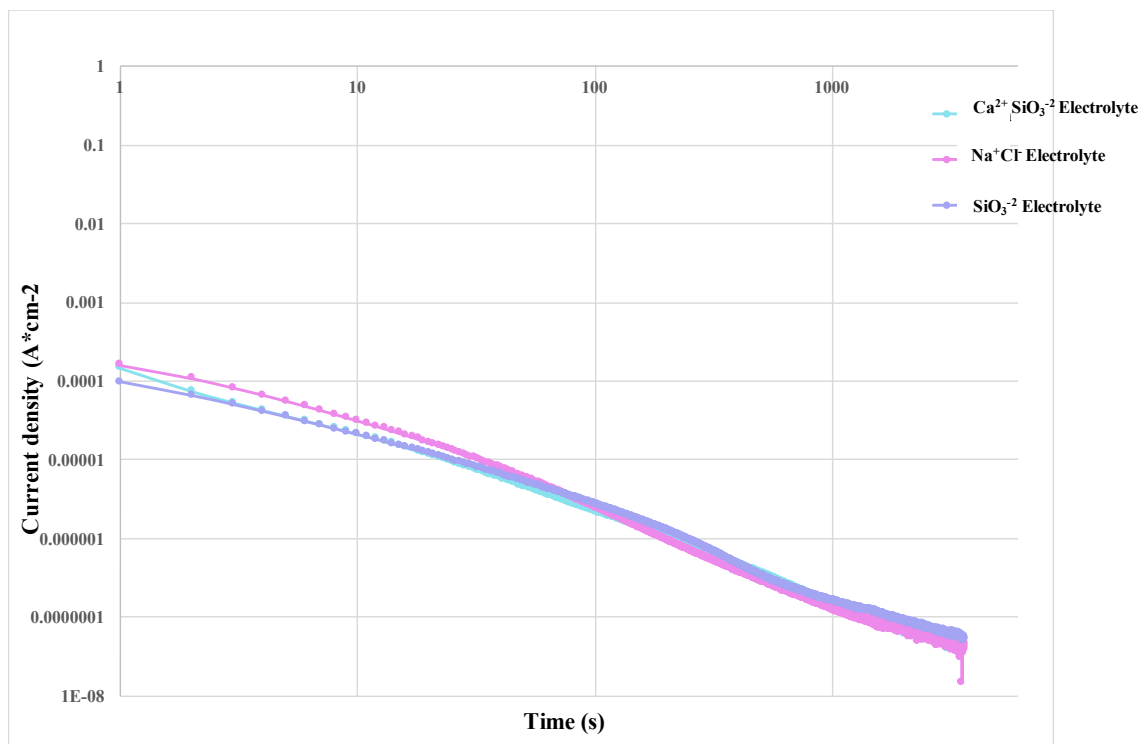
Figure 20. Potentiostatic current versus time curve of the UO_2 deposited electrode in contact with Na^+Cl^- 0,1 M pH=12; SiO_3^{-2} 0,001M pH=12 and SiO_3^{-2} 0,001M Ca^{2+} 0,0001 M pH=12 electrolytes

5.3 E_{corr} results

Next the E_{corr} results are shown. The system evolves from the cleaning cathodic potential applied to the electrode (-1.4V) to reach the ending state.

In the figure 21, the behavior of the corrosion potential in the presence of the Na^+-Cl^- electrolyte is very unstable, in the first 5,5 hours the potential increase, but in the following hours the potential decreased reaching a value of 0 mV. In the last 2 hours of experimental time, the potential reached a value of 42 mV approximately, but we cannot assure a steady state potential value. This result can be compared with the one obtained by Shoesmith et al., (1989) where the study of UO_2 in O_2-saturated atmosphere in a $NaClO_4$ 0,1 M dissolution pH=9,5 was performed; XPS analyses showed that two films formed. The first layer of $UO_{2,33}$ formed in the first 10 h of exposure, the outer layers of this film were converted, slowly, into hydrated UO_3 over the 90 h of the experiment. Under these conditions, the E_{corr} reached a steady-state value of 49 mV vs. Ag/AgCl, which is very close to the one obtained in the experiment.

Respect to the SiO_3^{-2} electrolyte, in the first 3 hours the potential value decrease in almost linear tendency. In the following hours, the behavior is unstable until the

46

potential reached a steady state value of 40 mV approximately. This value is very close to the potential value obtained in the experiment with the Na^+-Cl^- electrolyte. According to Shoesmith (2007) this might be due to a deposition of U^{VI} on the fuel surface. This deposit works as an insulator, it would be expected to block the fuel corrosion process occurring on the underlying conductive UO_{2+x} layer. It appears that de Si dissolution contribute to this process.

Finally, the SiO_3^{-2}, Ca^{2+} dissolution exhibits a behavior similar to the SiO_3^{-2} dissolution, but the potential value at the steady state is lower compared to the SiO_3^{-2} value, -2 mV, as it is shown in the figure 21. This can point to the oxidation, dissolution and the accumulation of corrosion products deposits on the electrode surface, this process might be reinforced by the presence of the Si and Ca in the dissolutions.
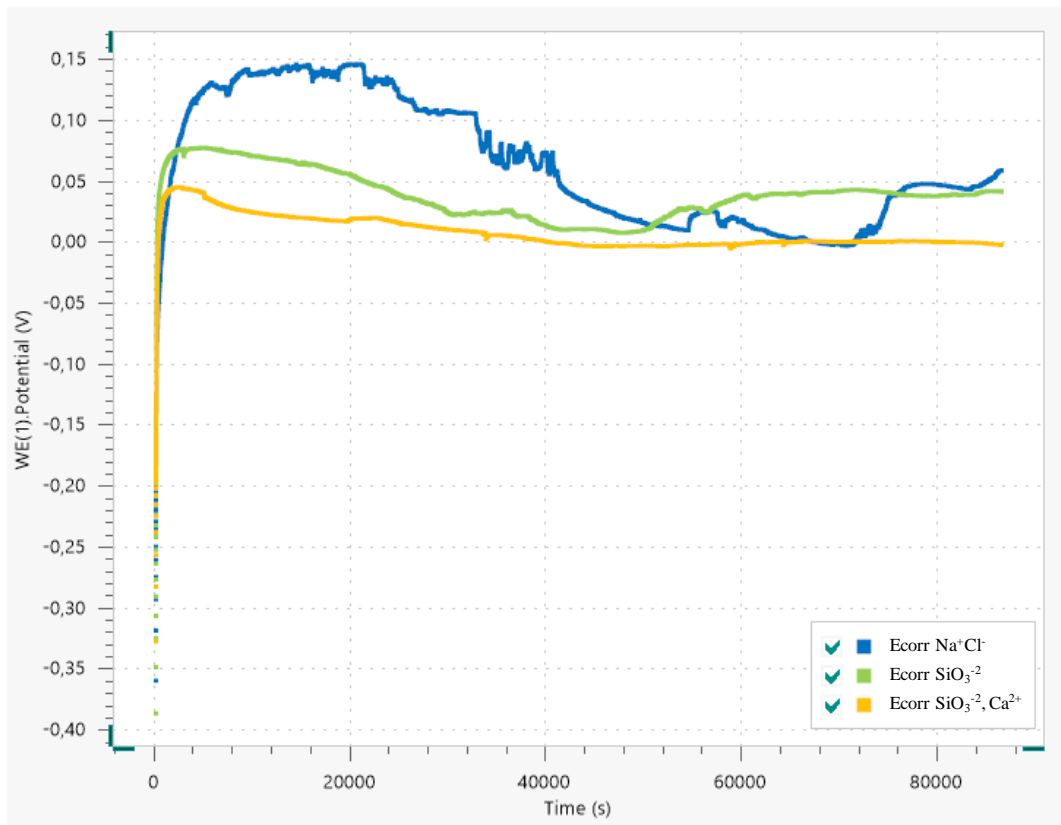
Figure 21. E_{corr} (V vs. Ag/AgCl) results on the modified electrode with UO_2 in contact with the three different electrolytes. Na^+Cl^- (blue line), SiO_3^{-2} (green line) and SiO_3^{-2}, Ca^{2+} (yellow line).

6. Conclusions

A review of the procedure for electrodeposition of the UO_2 has been used to modify a commercial electrode (Dropsens) surface.

After the UO_2 stripping, a corrosion study has been performed under oxidizing conditions in order to verify the behavior of the electrode modified. Three different electrolytes were used simulating the cementitious water.

Scanning electron microscopy (SEM) was used to analyze the surface of the electrodes, these images of the modified Dropsens exhibit differences between the 15 minutes' and 60 minutes' deposition time. For the first case, the surface was substantially modified, it appears to be a fractured surface with porous edges. For the second case, the electrode surface is very porous compare to the first case.

A Raman microscopy analysis was done to the modified surface of the electrode. The spectrum shows some peaks in the 249 (cm^{-1}) and 750 (cm^{-1}) Raman shift, according to the bibliography this spectrum is similar to the Raman spectrum exhibits by the U_3O_8 (Elorrieta et al. 2017).

Cyclic-voltammetry measurements showed that the electrode modified using 60 minutes of deposition time exhibits the most reproducible behavior respect to the 15 minutes' deposition time. As a consequence, the first modified electrode was used to perform the rest of the experiments.

Also, the cyclic-voltammograms obtained were divided into 6 regions: in the first region, the oxidation of non-stoichiometric UO_{2+x} is observed on the modified electrode. In the second region, the modified Dropsens exhibits a large oxidation that might be caused by various oxidation processes, precipitacion of U^{VI}. This oxidation process might be mitigated by the presence of the Si and Ca dissolutions. The third region exhibits a surface oxidation due to the accumulation of protective corrosion products deposits, which is reinforced by the presence of the Si and Ca dissolutions. The fifth region might be due to the presence of impurities and the final region, where the $UO_3 \cdot yH_2O \rightarrow UO_{2+x}$ reduction process is observed.

The potentiostatic experiments show that the highest current density was obtained for SiO_3^{-2} and Ca^{2+}, SiO_3^{-2}, and the lower current density was obtained for Na^+Cl^-. This information is corroborated by the cyclic-voltammograms results.

According to the E_{corr} results, the steady state potential value obtained with the Na^+Cl^- was 42 mV, very close to the value found by Shoesmith et al. (1989) under oxidizing conditions: 49 mV vs. Ag/AgCl. Respect to the SiO_3^{-2} electrolyte, the steady state value was 40 mV, very close to the Na^+Cl^- value, due to a deposition of U^{VI} on the fuel surface, this layer works as an inhibitor, blocking the fuel corrosion process.

The SiO_3^{-2}, Ca^{2+} electrolyte had a corrosion potential value at the steady state of -2 mV. At this potential, the presence of the Si and Ca dissolutions can reinforce the formation of protective corrosion products on the surface electrode.

7. Bibliographic References

- ASTUDILLO, J. (2001). *El almacenamiento geológico profundo de los residuos radiactivos de alta actividad. Principios básicos y tecnología.* ENRESA, Ed. ENRESA, Madrid. pp: 200.

- Berner, U. R. (1992). Evolution of pore water chemistry during degradation of cement in a radioactive waste repository environment. *Waste Management, 12*, 201-219.

- Burns PC, Klingensmith AL (2006). Uranium mineralogy and neptunium mobility. *Elements 2*, 351-356.

- Bruno, J., Ewing, R. C. (2006). Spent Nuclear Fuel. *Elements (2)*, 343-349.

- CHALMERS, J. M., EDWARDS H. G. M., HARGREAVES M. D. (2012). *Infrared and Raman Spectroscopy in forensic science.* United Kingdom. John Wiley & Sons Ltd.

- Chusuei, C. C., Goodman, D. W. (2002). X-Ray Photoelectron Spectroscopy. *Encyclopedia of Physical Science and Technology 17*, 921-938.

- Consejo de Seguridad Nuclear, Gobierno de España. (2015). El combustible nuclear y su ciclo: Almacenamiento temporal centralizado. https://www.csn.es/es/almacenamiento-temporal-centralizado.

- De Pablo, J., Casas, I., Giménez, J., Marti, V., & Torrero, M. E. (1996). Solid surface evolution model to predict uranium release from unirradiated UO 2 and nuclear spent fuel dissolution under oxidizing conditions. *ELSEVIER Journal of Nuclear Materials*, *232*, 138–145.

- EGERTON, R. F. (2005). *Physical Principles of Electron Microscopy*: *An introduction to TEM, SEM and AEM.* Alberta, Canada. Springer Science+Business Media Inc. pp:125-153.

- Elorrieta, J. M., Bonales, L. J., Rodríguez, N., Gutiérrez, L., Cobos, J., & Baonza, V. G. (2017). Estudio de la oxidación de la matriz del combustible irradiado en condiciones de almacenamiento en seco, *8*, 1–8.

- Escribano, R., Sloan, J. J., Siddique, N., Sze, N., & Dudev, T. (2001). Raman spectroscopy of carbon-containing particles, *26*, 179–186.

- Fernández, R. (2011). Technical Note: Engineered barriers for radioactive waste confinement. *Materiales de Construcción, 61*(303), 485-492.

- Gens, R. (2008). *Formulation of the concrete for the modules, concrete containers and the cementitious backfill.* NIROND 2007-1876.

- GOLDSTEIN, J., NEMBURY, D., JOY, D., LYMAN, C., ECHLIN, P., LIFSHIN, E., SAWYER, L., MICHAEL J. R. (2003). *Scanning Electron Microscopy and X-ray Microanalysis.* Springer US. pp: 1-2.

- *Electrochimica Acta*, *51*(16), 3278–3286. http://doi.org/10.1016/j.electacta.2005.09.019

- GRENTHE, I., FUGER, J., KONINGS, R. J., LEMIRE, R. J., MULLER, A. B., NGUYEN-TRUNG, C. and WANNER, H. (1992). *Chemical thermodynamics of uranium.* Amsterdam, Holland.

- Harfouche, M., Wieland, E., Dähn, R., Fujita. T., Tits, J., Kunz, D. and Tsukamoto, M. (2006). EXAFS study of U(VI) uptake by calcium silicate hydrates. *Journal of colloid and interface science, 303*(1), 195-204.

- IAEA. (2006). Storage and Disposal of Spent Fuel and High Level Radioactive Waste. *Nuclear Energy*, (February), 1–11. Retrieved from https://www.iaea.org/About/Policy/GC/GC50/GC50InfDocuments/English/gc50inf-3-att5_en.pdf

- IAEA. (2009). Costing of Spent Nuclear Fuel Storage. *Nuclear Energy Series*, (NF-T-3.5).

- Jensen, R. T. (1983). Inventories and characteristics of transuranic waste. *Nucl. Chem. Waste management, 4*(1), 19.

- Jonhson, L.H., Leneveu, King, F., D. M., Shoesmith, D. W., Kolar, M., Oscarson D. W., Sunder, S., Onofrei, C. and Crosthwaite, J.L. (1996). The disposal of Canada's nuclear fuel waste: A study of post closure safety of in-room emplacement of used CANDU fuel in cooper containers in permeable plutonic rock volume 2: Vault model. Atomic Energy of Canada Limited Report, AECL-11494-2, COG-95-552-2.

- Jonhson, L. H., Werme, L. O. (1994). Materials characteristics and dissolution behavior of spent nuclear fuel. MRS Bulletin. pp: 24-27.

- JOVANI-ABRIL, R. (2014). *Synthesis and characterization of nanocrystalline UO$_2$ ceramics.* Universidad de Santiago de Compostela (USC), Spain.

- Keith, S. K., Faroon, O., Roney, N. R., Scinicariello, F., Wilbur, S., Ingerman, L., Diamond, G. (2013). Toxicological Profile for Uranium. *Toxicological Profiles*, (February), 1–526. http://doi.org/http://dx.doi.org/10.1155/2013/286524

- Kissinger, K., Heineman, W. (1983). Cyclic Voltammetry. *Journal of chemical education. 60*(9), 702-706.

- Nagra, Project Opalinus Clay-Safety Report, Nagra Technical Report NTB 02-05, Wettingen, Switzerland, 2002.

- PÉREZ, N. (2004). *Electrochemistry and Corrosion Science*. Boston, USA. Kluwer Academic Publishers. pp: 1-6.

- RONCHI, C.; LOSILEVSKI, I.; YAKUB, E. (2011). *Equation of State of Uranium Dioxide: Data Collection.* Berlin, Germany. Springer Science & Business Media. pp: 1-2.

- Rojo, I., Rovira, M., De Pablo, J. (2014). Selenate Diffusion Trough Mortar and Concrete. *Environmental Engineering Science, 31*(8), 469-473.

- SALING, J. H., FENTIMAN, A. W., TANG, Y. S. (2001). *Radioactive waste management Second Edition.* Michigan, United States. Taylor & Francis.

- Santos, B. G., Noël, J. J., & Shoesmith, D. W. (2006). The effect of pH on the anodic dissolution of SIMFUEL (UO2). *Journal of Electroanalytical Chemistry*, *586*(1), 1–11. http://doi.org/10.1016/j.jelechem.2005.09.021.

- Santos, B. G., Noël, J. J., Shoesmith, D. W. (2006b). The influence of silicate on the development of acidity in corrosion product deposits on SIMFUEL (UO$_2$). *Corrosion Science, 48*, 3856-3868.

- Santos, B. G., Noël, J. J., Shoesmith, D. W. (2006c). The influence of calcium ions on the development of acidity in corrosion product deposits on SIMFUEL (UO$_2$). Journal of *Nuclear Materials, 350*, 320-331.

- Swapp, S. (2017). Scanning Electron Microscopy (SEM). University of Wyoming, United States. Recovered from: http://serc.carleton.edu/research_education/geochemsheets/techniques/SEM.html.

- SETTLE, F. A. (1997). *Handbook of instrumental techniques for analytical chemistry.* New Jersey. Prentice, Inc.

- Shoesmith, D. W. Sunder, S., Bailey, M. G., Wallace, G. J. (1989). The Corrosion of nuclear fuel (UO2) in oxygenated solutions. *Corrosion Science*, *29*(9), 1115–1128.

- SHOESMITH, D. W. (2007). *Used fuel and uranium dioxide dissolution studies-Review*. Nuclear-Waste Management Organization. The University of Western Ontario. Ontario, Canada.

- Shoesmith, D. W., & Sunder, S. (1991). Electrochemistry-based model for the dissolution of UO$_2$. *Atomic Energy of Canada Limited, AECL (Report)*, (10488), 1–97.

- Shoesmith, D. W. (2000). Fuel corrosion processes under waste disposal conditions. *Journal of Nuclear Materials*, *282*(1), 1–31. http://doi.org/10.1016/S0022-3115(00)00392-5.

- SKOOG, D. A., HOLLER, F. J., CROUCH, S. R. (2007). *Principles of instrumental analysis*. Thomson Brooks/Cole.

- Sunder, S., Shoesmith, D. W., Lemire, R. J., Bailey, M. G., Wallace, G. J. (1991). The effect of pH on the corrosion of nuclear fuel (UO_2) in oxygenated solutions. *Corrosion Science, 32*(4), 376-386.

- UK National Physical Laboratory. (2012). X-ray photoelectron spectroscopy: Surface and nanoanalysis basics. Recovered from: http://www.npl.co.uk/science-technology/surface-and-nanoanalysis/surface-and-nanoanalysis-basics/introduction-to-xps-x-ray-photoelectron-spectroscopy.

- Wang, Y., Alsmeyer, D. C., & Mccreery, R. L. (1990). Raman spectroscopy of carbon materials: Structural basis of observed spectra. *Carbon*, (10), 557–563.

- Watts, J. F. (1994). X-ray photoelectron spectroscopy. *Vacuum 45*(6), 653-671.

- WILLARD, H. H., MERITT Jr L. L., DEAN J. J., SETTLE Jr. F. A. (1988). *Instrumental methods of analysis.* 7th ed. New Delhi, India. CBS Publisher & Distributors.
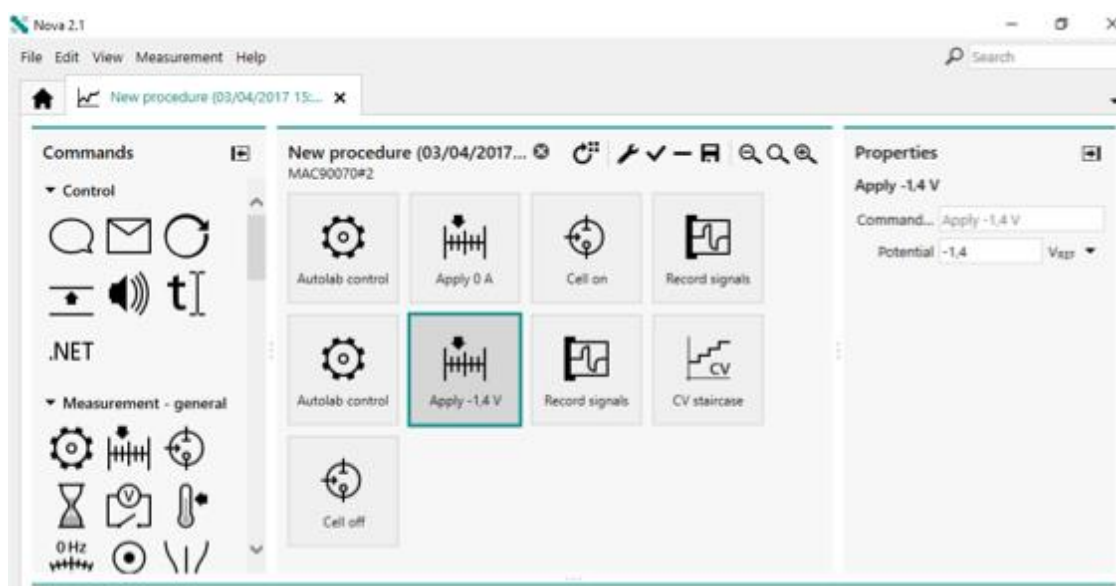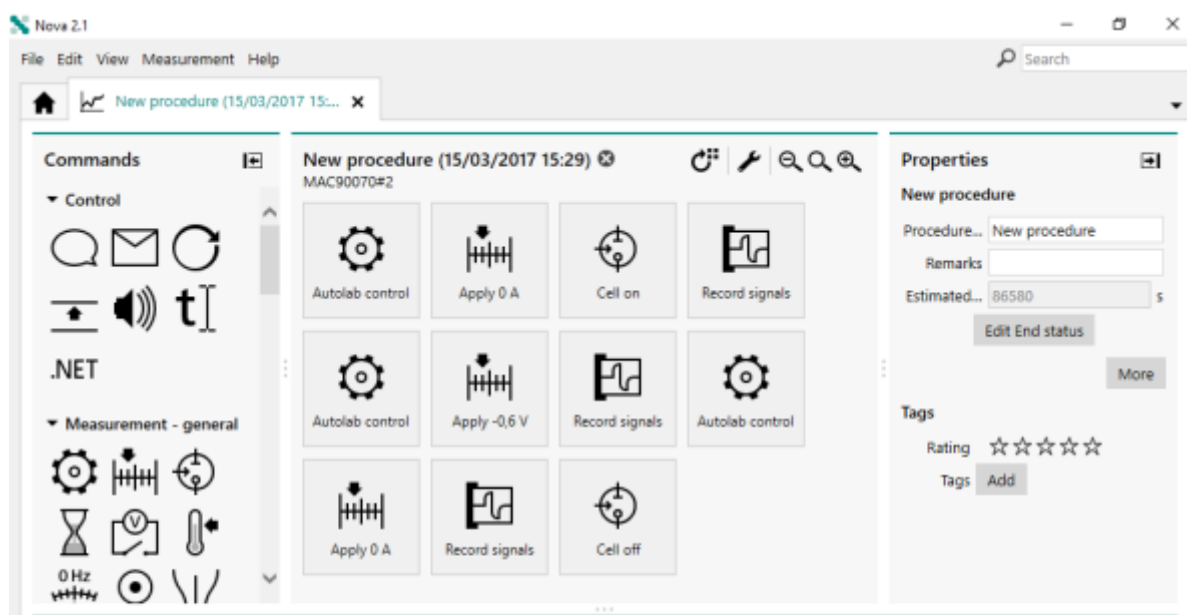
8. Annexes

## Annexe 8.1 Procedures used to perform the electrochemical studies.
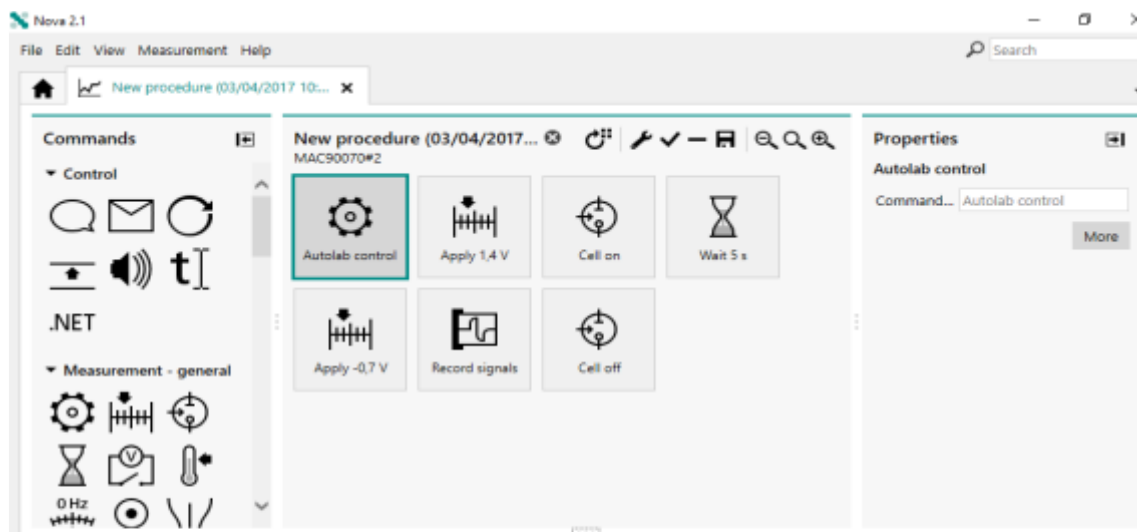
Figure 22. Electrodeposition procedure using NOVA software 2.1 coupled with the Metrohm Autolab Potentiostat-Galvanostat M204.

Figure 23. Cyclic-voltammogram procedure using NOVA software 2.1 coupled with the Metrohm Autolab Potentiostat-Galvanostat M204.

Figure 24. OCP procedure using NOVA software 2.1 coupled with the Metrohm Autolab Potentiostat-Galvanostat M204.
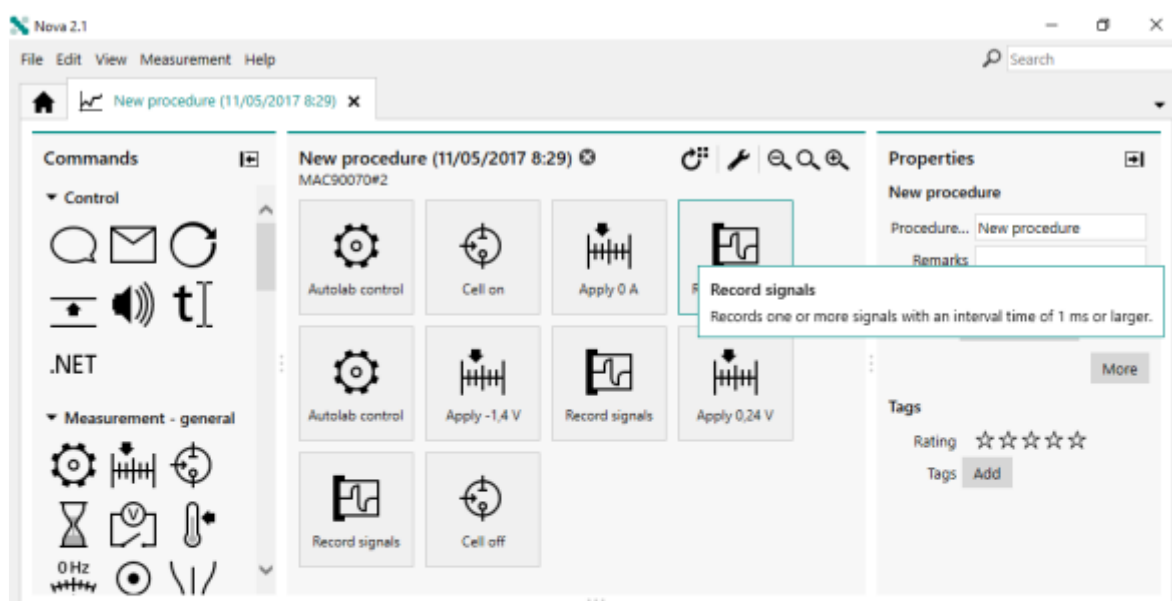
Figure 25. Potentiostatic experiment procedure using NOVA software 2.1 coupled with the Metrohm Autolab Potentiostat-Galvanostat M204.